A 2D microfluidic model of cerebrospinal fluid motion in periarterial spaces

by

Sasha Toole

A thesis submitted to the Department of Physics
in partial fulfillment of the
requirements for the degree of
Bachelor of Arts in Physics

South Hadley, Massachusetts
May 19, 2024

Approved by

Kerstin Nordstrom, Associate Professor of Physics, Mount Holyoke College
Spencer Smith, Associate Professor of Physics, Mount Holyoke College
Kenneth Colodner, Associate Professor of Neuroscience and Behavior, Mount Holyoke College

Abstract

The glymphatic system is a pathway for metabolic waste clearance in the brain. In a crucial step of this pathway, cerebrospinal fluid (CSF) enters the brain via periarterial spaces. Previous studies in live mice have found that peristaltic waves in the arterial wall, driven by pulsatile blood flow, can induce the flow of CSF in the surrounding periarterial space. However, the exact mechanism driving CSF flow remains unclear among multiple possible contributing mechanisms. We developed a microfluidic device that serves as a two-dimensional model of the arterial wall interface between the periarterial space and inner artery to study the flow of peristaltically driven CSF. With this microfluidic model, we tested pulsation frequencies motivated by human, rat, and mouse heart rates and observed trends in both the oscillatory and bulk components of the model CSF flow. We additionally observed a relationship between the approximate membrane waveform and the fluid motion in the model periarterial space. These observations contribute new insight to the understanding of CSF flow mechanisms.

Acknowledgments

I would first like to thank Professor Kerstin Nordstrom for working with me on this project over the past two years. I would not have been able to complete this thesis without her guidance. Her mentoring pushed me to grow into the researcher I am today. Thank you for all of your endless support and for believing in me when I didn't.

I would like to thank Professor Spencer Smith, both for his support on my thesis committee and for his guidance in the classroom. Taking Math Methods with him helped lay the foundation for my physics education. I would also like to thank Professor Ken Colodner. Thank you for your support on my thesis committee and for your insightful suggestions during the defense.

I would like to thank Dr. Lori McCabe for all of her help in the lab, from camera setup to Cricut cutting adventures. Her help with technical lab troubleshooting, comments on practice presentations, and the advice you gave along the way were invaluable. Thank you for helping make this thesis happen.

I would like to thank everyone who has been a part of the Nordstrom CRAM lab these past two years with me. To Shanen Arellano, Giselle Dencker, Ama Abrokwa, Mao Yasueda, Latika Joshi, and Lucy Sternberg, thank you for being a part of this amazing research group with me. I have thoroughly enjoyed our lab chats and watching your weekly group meeting update presentations. To Abigail Tadlock and Anna Maria Moran, thank you for setting the standard for an amazing honors thesis project. Watching your thesis progress during group meetings last year as well as attending your Senior Symposium and thesis defense practice talks and presentations was more helpful than you can imagine! I have been grabbing your theses off the shelf when I feel lost. Thank you so much for your guidance. I hope you are off doing amazing things in graduate school.

To Ella Phillips, thank you for being there with me since the beginning. I can't believe we have known each other since taking 201 together, both of our first in-person physics classes at Mount Holyoke. We've come a long way since the early days of taking 201 and 220 together as underclassmen. It's been such a pleasure to learn physics together and to co-TA in my final semester. My life is so much more "slay" and "yippee" knowing you. I can't wait to see you around in Boston this summer.

To MJ Khan, thank you for being the kingliest king around. It has been a pleasure to serve on the Society of Physics Students board with you together these past two years. I'm so glad you encouraged me to run for secretary two years ago as being on the board has brought us together. I will forever look back fondly on our physics lounge shenanigans and purple man filled memories. Your hard work and intellect continue to inspire me every day. I am confident you will excel at Vanderbilt these next few years.

To Reece Liu, thank you for roughing it with me at UMass this semester. I would not be surviving Electricity and Magnetism without you there. I have had so much fun taking physics classes with you these past few years and inadvertently being your 220 TA this past semester. And how could I forget all of our fun times climbing (you too Ella)! I'm looking forward to starting our next chapters moving to Boston together. You're going to do amazing things at Tufts.

To Helen Frank, thank you for being such an amazing friend. I have had so much fun taking physics classes with you and traveling across Germany and the Netherlands together. It is always my pleasure to serve as your international navigator. I know you're out doing great things abroad in Germany right now. I can't wait to see where life takes you over your final year and beyond!

To Sam Nielsen, my biggest cheerleader, thank you for holding me together over the final stretch. You've stayed there with me through every tough moment and for every late night. I seriously would not have made it to the finish line without you. I cannot thank you

enough! I'm so excited to start graduate school with you in the fall at Brandeis. Soft matter warm girls forever!

To my parents, thank you for being there for me since the beginning. You've always believed I would do great things. And look at me now! Your endless support has pushed me to new heights. And to Lily, my sister, keep being you. You're doing amazing things over your first year at Dickinson and I'm so proud of you! Thank you for being my sister. I can't wait to see you all again as a new college graduate.

Contents

List of Figures

List of Tables

Chapter 1

Introduction

1.1 The Glymphatic System

1.1.1 General Overview

The brain has many roles orchestrating the functions of the cardiovascular, respiratory, metabolic, motor, and autonomic nervous systems. This generates a high energy demand such that for humans, the brain accounts for 20% of oxygen use despite accounting for only 2% of body mass [1]. The brain's energy needs require the transport of large quantities of nutrients, such as glucose [2], into the brain, and its cellular activity likewise generates waste metabolites at a higher rate than other organs [3]. Clearance of waste metabolites is necessary to maintain homeostasis as waste protein aggregation may contribute to neurodegenerative disease [4].

The lymphatic system is the primary method of waste removal for most tissues in the body. In the lymphatic system, fluid flow in the interstitium drives waste removal into the lymph vessels. The interstitium, or interstitial space, is the extracellular space outside of cells, blood vessels, and lymph vessels [5]. Fluid leaks through arterial walls and slowly flows across the interstitial space surrounding the tissue's cells, delivering nutrients and providing hydration to the cells. Cells transport wastes into the interstitial fluid, which is collected in the lymph vessels for clearance into the venous circulation and eventually the liver and kidneys [3].

Despite the direct correlation of tissue metabolic rate and lymph density elsewhere in the body [6], the central nervous system (CNS), comprising the brain and spinal cord, lacks a lymphatic system. Wastes must therefore be removed from the brain by alternate means.

Most protein wastes in the brain are removed by intracellular processes, namely proteasomal degradation and autophagy [7]. However, many waste proteins are removed from cells and into the interstitial space of the brain [8], suggesting that there must also be an extracellular waste removal mechanism at play.

The roles of two fluids have been studied in extracellular brain waste removal: cerebrospinal fluid (CSF) and interstitial fluid (ISF). CSF is a clear and colorless mixture of water, proteins, ions, neurotransmitters, and glucose occupying the cerebral and spinal subarachnoid spaces, the ventricular system, and the perivascular spaces of the CNS [9]. CSF has important functions in the brain including nutrient delivery and waste removal, cushioning the brain, and compensating for blood volume fluctuations during the cardiac cycle [10]. ISF has a similar composition to CSF and occupies the interstitium. ISF provides a medium through which cells exchange oxygen, nutrients, and wastes and is a key component of waste clearance into the lymphatic system. The regulation of ion concentrations and osmolality in ISF is also important for nervous activity and cell volume maintenance respectively [11].

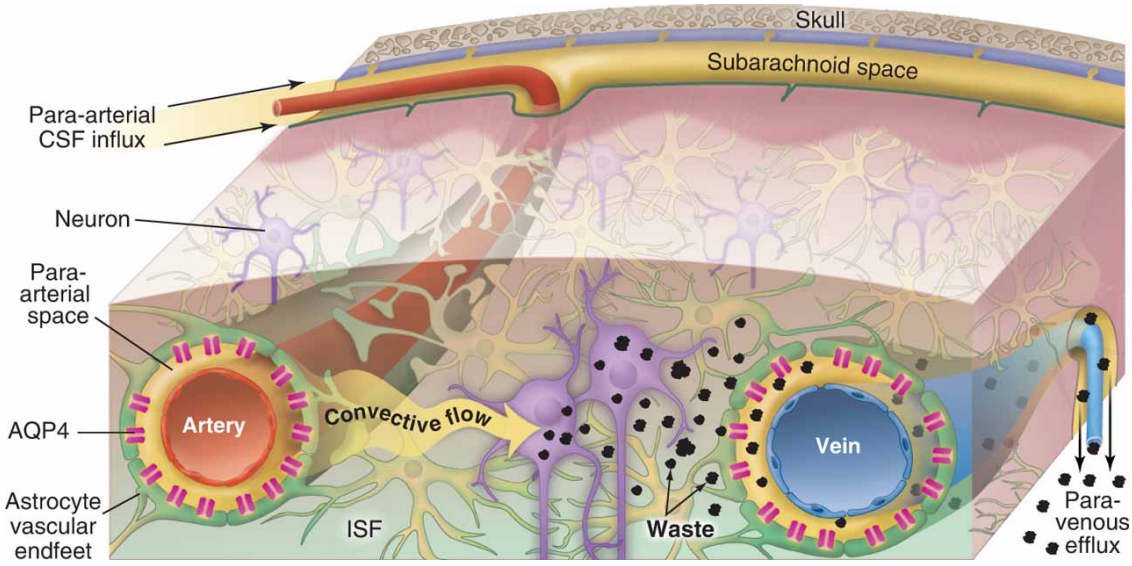

Figure 1.1: Pathway of the glymphatic system. CSF influx occurs through periarterial spaces (left), and ISF efflux occurs through peravenous spaces (right). The two flows are coupled through the interstitial space (middle), where waste proteins have accumulated, via astrocytes surrounding the blood vessels [13].

Recent experiments have found that the flows of CSF and ISF in the brain contribute to a larger waste clearance system. Iliff *et al.* [12] used two-photon imaging in live mice to map the flows of CSF and ISF and the transport of waste solutes in the brain. They found that CSF and ISF exchange in a brain-wide waste removal system, proposed as the glymphatic system. Their glymphatic hypothesis comprises three key components: CSF influx via periarterial spaces, ISF efflux via perivenous spaces, and a route that couples the two perivascular flows in the interstitial space [12]. The waste clearance system was termed the "glymphatic" system after its analogy to the lymphatic system and its dependence on aquaporin-4 (AQP4) glial water channels [13]. Figure 1.1 summarizes the pathway of the glymphatic system.

CSF is produced in the choroid plexus, a group of blood vessels and cells found in each ventricle of the brain, and travels through periarterial spaces, annular spaces surrounding arteries bound by the arterial wall of the blood vessel and the apical processes of astrocytes. The vascular endfeet of the astrocytes have AQP4 water channels, facilitating CSF flow from periarterial spaces into the interstitial space [14], the ISF-filled space between blood vessels and cells in the brain. Bulk flow of CSF into the interstitial space drives accumulated wastes away from incoming arteries and toward outgoing veins. ISF and its constituent wastes flow into peravenous spaces, the venous analog of periarterial spaces, via AQP4 channels on the surrounding astrocytes. Through the peravenous space, waste-carrying ISF travels out of the brain and into the lymph vessels of the neck, where wastes are ultimately processed in the liver and kidneys. Each of these three flows is uniquely driven and therefore requires separate study. This study focuses on mechanisms of periarterial CSF influx.

1.1.2 Flow in Periarterial Spaces

Periarterial spaces exist around arteries and are bounded by the outer arterial wall and the endfeet of surrounding astrocytes (Figure 1.2). The astrocytic endfeet contain AQP4 trans-membrane water channels important for CSF flow into the interstitial space [15].

Measurements using two-photon imaging reveal periarterial spaces in mice are estimated to be 40 μm wide [16], comparable to the width of the adjacent artery.

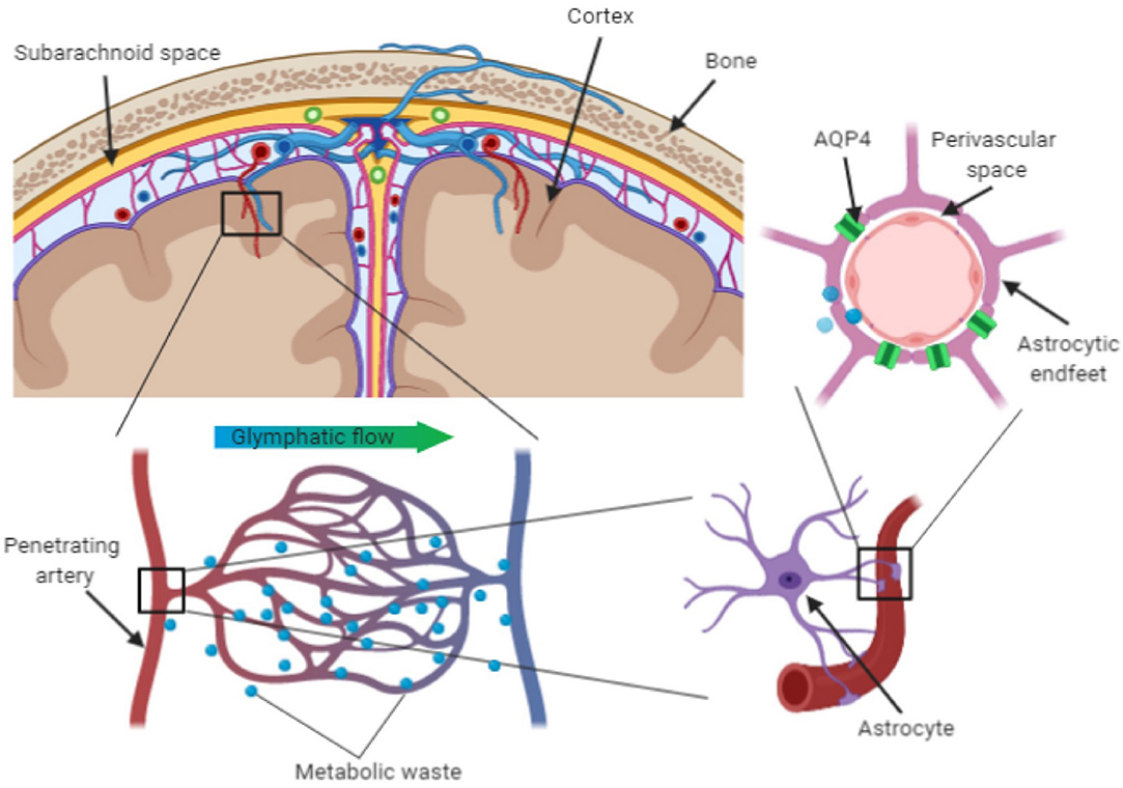

Figure 1.2: Zooming in on the periarterial space. Top left: Cross-section of the brain. Bottom left: Zooming in on an artery and vein penetrating the cortex. Glymphatic flow starts at the penetrating artery and moves across the interstitial space toward the penetrating vein. Bottom right: Zooming in on the artery. Astrocytic endfeet surround the penetrating artery. Top right: Zooming in on the periarterial space. Cross-section of the penetrating artery showing the periarterial space formed between the arterial wall and surrounding astrocytic endfeet [17].

The shape of periarterial spaces can vary across species and location in the brain [17]. Observations of periarterial spaces show they form oblong spaces around arteries that are not perfectly annular. The hydraulic resistance of flow within periarterial spaces decreases as the cross-sectional area increases [18], so geometry may be an important factor in periarterial flow. Computations show that an elliptical periarterial shape surrounding a circular artery minimizes hydraulic resistance [19], therefore optimizing flow speeds within the periarterial

space. These results suggest the concentric circular models used in some computational simulations are a poor representation of perivascular spaces and could explain some discrepancies between computation and experiment.

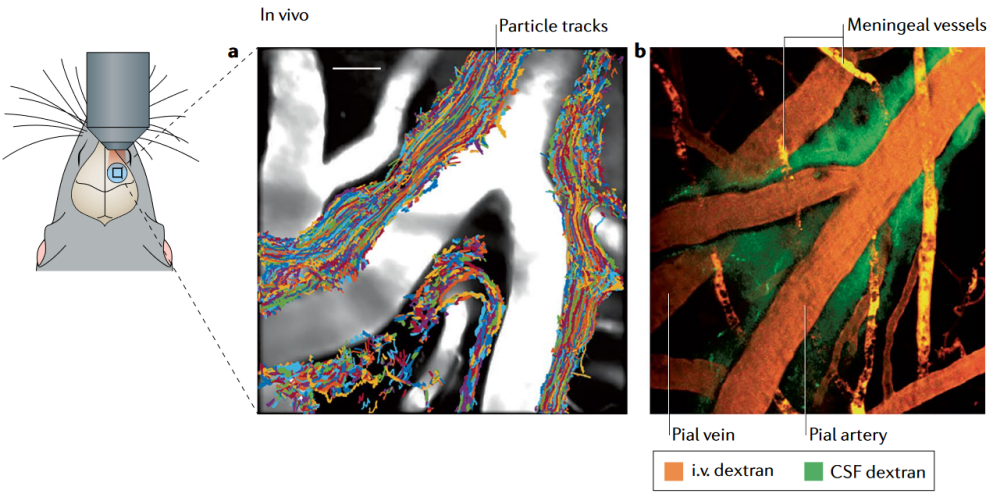

Figure 1.3: Two photon imaging in live mice shows the flow of cerebrospinal fluid in periarterial spaces. (a) Particle tracks (multi-color) from CSF tracer flow show fluid motion in the area surrounding arteries (white). (b) Fluorescent dextran confirms the location of the artery (orange) and the presence of CSF (green) in the surrounding periarterial space. Adapted from [16] by [21].

CSF influx in the glymphatic system occurs through periarterial spaces. In vivo two-photon imaging is used to quantify this flow in mice through a cranial window (Figure 1.3). Quantified CSF flows show periarterial spaces form open channels [20]. In mice, periarterial transport of tracer particles is ballistic, indicating an open space, rather than diffusive, which would suggest the periarterial space is filled with a spongy, porous medium (Figure 1.4a). Comparisons between experiment and theory further support that periarterial spaces are open. Time-averaged velocity profiles of periarterial flow match closely with theoretical velocity profiles for Poiseuille flow (see Section 1.2.1) in an open-space model and disagree with theoretical velocity profiles for flow in a porous medium model (Figure 1.4b).

The net flow of CSF in periarterial spaces occurs in the direction of adjacent arterial blood flow [16, 22, 23]. While this is the current consensus, there has been some controversy over the direction of CSF flow. Early experimental work used fixed tissues to observe CSF

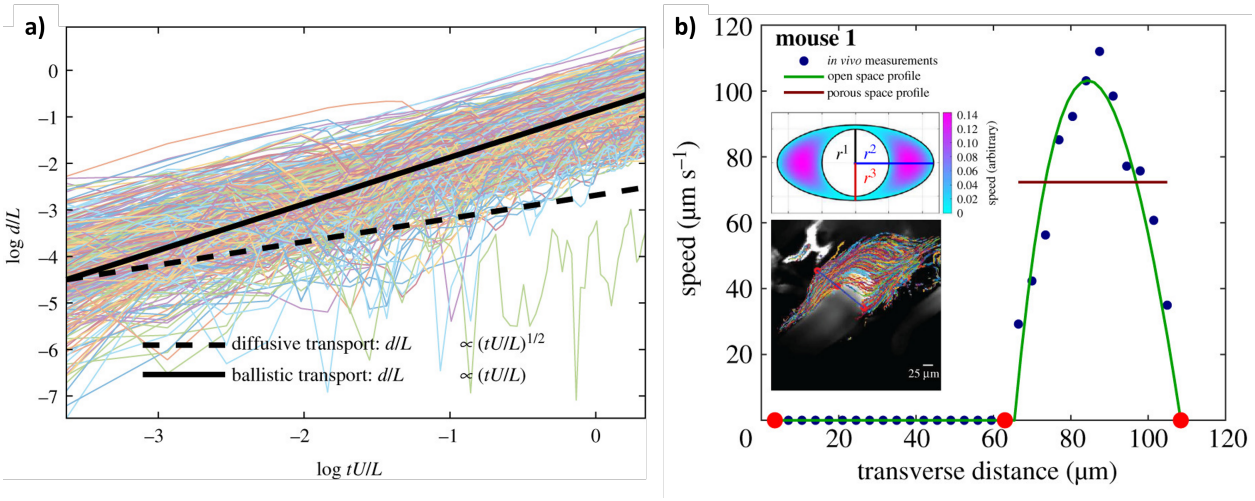

Figure 1.4: Periarterial spaces are open, not porous. (a) Particle tracks from periarterial flow closely follow smooth, ballistic motion characteristic of an open channel. (b) Time-averaged velocity profiles of periarterial flow measured in vivo match closely with a theoretical open-space model but not with a porous medium model. Adapted from [20].

flow. These studies observed CSF tracers in the basement membranes of arteries and periarterial flow in the opposite direction as blood flow, both of which conflict with in vivo results. The tissue fixation process was found to be the cause of these conflicting results. Mestre *et al.* [16] observed that perfusion fixation of tissue with paraformaldehyde resulted in the periarterial spaces shrinking and therefore caused the retrograde flow observed by earlier experiments. They found that the cross-sectional area of periarterial spaces in fixed tissues shrank to 0.14 times that of the artery compared to 1.4 times for in vivo measurements [16]. In vivo experimental work is therefore important for accurately studying periarterial flow.

There has also been controversy regarding the impacts of tracer injection on periarterial flow, and whether observed flows are an artifact of tracer injection. Experimental work using a dual syringe setup, allowing for constant periarterial fluid volume, agrees with results from experimental work using a more common single-syringe setup. These results suggest that the bulk flow of CSF observed from in vivo experiments is not an artifact of tracer fluid injection [22].

1.1.3 Mechanisms of Periarterial Flow

The mechanism of CSF bulk flow in periarterial spaces is currently under debate. While the periarterial CSF flow is well characterized, the mechanism of CSF influx is unclear. The challenge of needing to perform in vivo experiments makes directly studying the mechanism periarterial flow difficult. There are currently many proposed physiological mechanisms being studied. The flowing section summarizes current research on three such mechanisms: arterial pulsations, sleep-wake cycles, and respiratory motion [21].

Arterial Pulsations

The heart pumps blood in a rhythmic fashion, and this pulsatile pumping of blood through arteries causes waves to propagate in the arterial wall. These waves periodically expand and contract the surrounding periarterial space, which could drive periarterial flow through a process known as peristalsis. This thesis explores the ability of arterial pulsations to drive periarterial CSF flow.

Early research by Hadaczek *et al.* [24] observed the effects of cardiac factors on convection-enhanced delivery drug infusion using rats. In the rats studied, infused molecules were primarily distributed in perivascular spaces [24], confirming that the distribution of infused molecules observed was due to perivascular transport. The authors compared perivascular transport between rats with high heart rates and rats with low or no heart rate. They found that the distribution of infused molecules is significantly greater for rats with high heart rates and blood pressures than for rats with low or no heart rate [24]. Compared to rats with no blood flow, rats with high heart rates have significantly greater perivascular transport. This provides evidence that cardiac contractions contribute to perivascular flow.

Later studies by Mestre *et al.* [16] and Bedussi *et al.* [23] used in vivo two-photon imaging to directly examine arterial pulsations as a mechanism of perivascular transport in mice. Both studies concluded that arterial wall motion is the principle driving mechanism of periarterial flow. They identified two components of periarterial flow. One component is

a constant flow in the direction of bulk blood flow with an average velocity of 20 μm/s. This component is the bulk flow of CSF in periarterial spaces. The second is an oscillatory flow with an average peak velocity of 10 μm/s and correlating adjacent arterial pulsations (Figure 1.5). This secondary flow is pulsatile, driven primarily by the cardiac cycle [16,23], and does not contribute to the bulk CSF flow. The oscillatory flow is shown to have a phase offset from the arterial wall motion of 353°. Mestre *et al.* additionally observed that hypertension, or high blood pressure, decreases periarterial flow in mice [16]. High blood pressure increases arterial wall stiffness, which could restrict the amplitude of peristaltic waves propagating in the arterial wall.

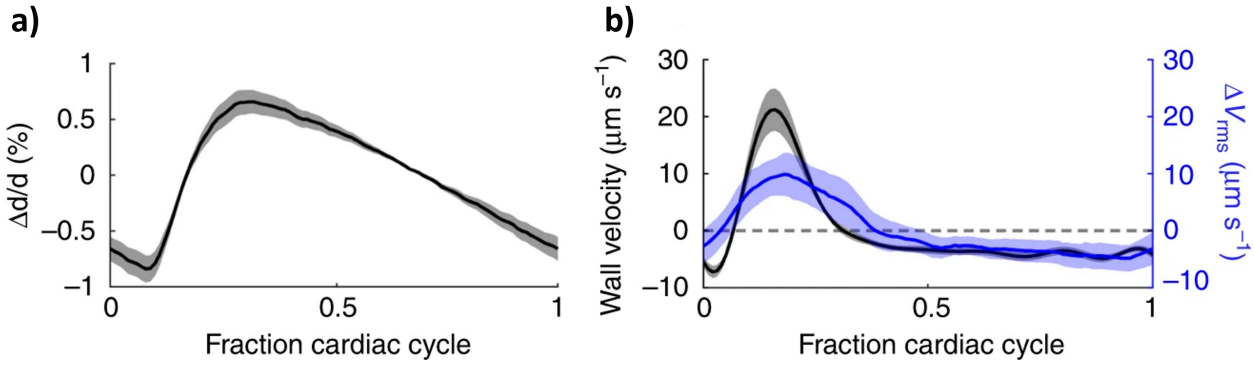

Figure 1.5: Experimental observations using in vivo two-photon imaging of mice shows arterial pulsations correspond with bulk periarterial flow. a) The normalized average change in artery diameter over the cardiac cycle. b) The arterial wall velocity (black curve) and change in root-mean-square velocity of CSF (blue curve) over the cardiac cycle [16].

Computational models of periarterial flow conflict with experimental results. A computational study by Kedarasetti *et al.* [25] using simulations of periarterial flow found that experimentally observed flows from Mestre *et al.* and Bedussi *et al.* could not be reproduced from arterial waves with physiologically-plausible amplitudes. They found that reasonable arterial pulsations can only drive oscillatory flow of CSF and not the directional pumping observed in experiments. The simulation required wave amplitudes much larger than is physiologically possible to reproduce experimental flows using only arterial pulsations as the driving mechanism (Figure 1.6). However, the simulation was able to reproduce the 20 μm/s flows found experimentally using reasonable arterial wall amplitudes when a constant

pressure gradient on the order of 0.01 mmHg/mm was introduced over the simulated 5 mm middle cerebral artery [25]. For context, this pressure gradient converts to 2 mmHg/m, which is similar to the 2.85 mmHg/m pressure gradient measured between the ventricular and subdural spaces in humans [26].

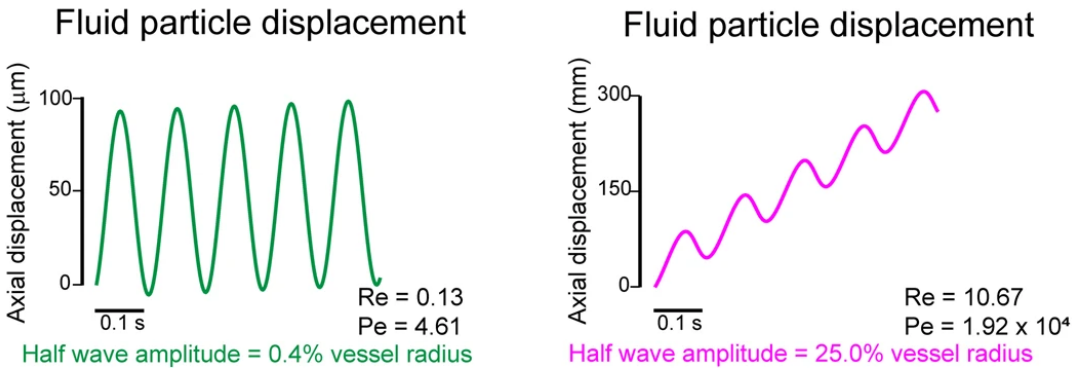

Figure 1.6: Displacement along the PVS vs. time for a computational model. Typical wave amplitudes of the arterial wall result in negligible bulk flow (left). An unphysiologically large wave amplitude 25% the artery radius is needed to replicate experimental results (right) [25].

Sleep-Wake Cycles

Sleep-wake cycles may also play a role in glymphatic clearance. In mice, clearance of CSF tracers is increased during sleep. Xie *et al.* found that the volume fraction of CSF tracers in the interstitial space is 22-24% in sleeping or anesthetized mice and 13-15% in awake mice [27]. Waste clearance by CSF into the interstitial space is therefore greatly increased in sleep states and suppressed in awake states (Figure 1.7). It is important to note that the volume fractions measured are very large, indicating that flow was non-Newtonian. The similar results found in sleeping and anesthetized mice also suggest the sleep-wake cycle itself, rather than circadian rhythm, is responsible for the changes in waste clearance observed. Similar results are found when measuring waste protein clearance. The waste protein amyloid-β (Aβ), associated with Alzheimer's disease, is cleared twice as fast in sleeping mice compared to awake mice [27], and wakefullness correlates with Aβ accumulation

in the ISF in mice [28]. This further supports the idea that sleep states increase glymphatic clearance while awake states decrease glymphatic clearance.

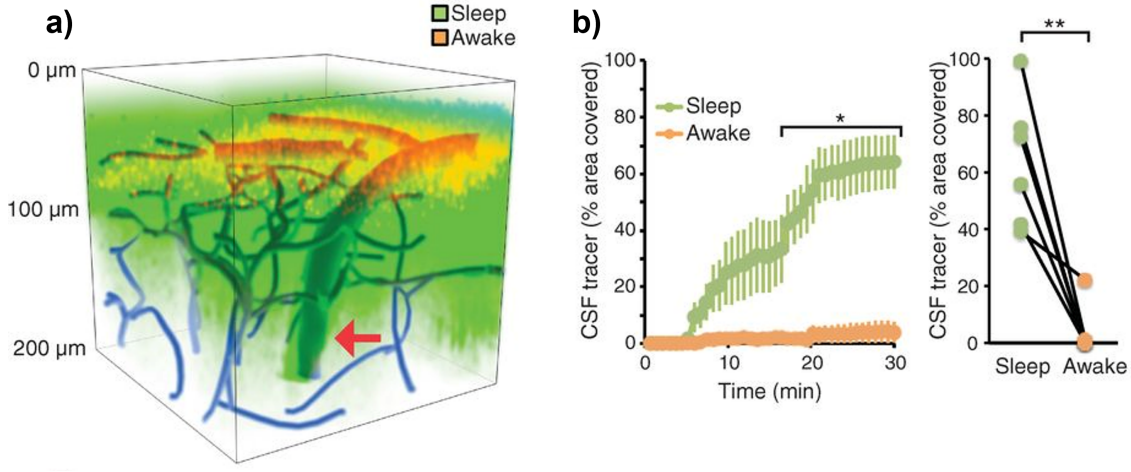

Figure 1.7: The influx of CSF tracers is suppressed in awake mice compared to sleeping mice. a) Three-dimensional distribution of CSF tracers in mice while asleep (green) compared to 15 minutes after waking (orange). The red arrow points to a penetrating artery. b) The percent area covered by CSF tracer over time is much greater in sleeping mice compared to awake mice [27].

Additionally, sleep deprivation decreases glymphatic clearance in both mice and humans. In mice, sleep deprivation results in an increased concentration of Aβ in the ISF, and chronic sleep restriction increases Aβ plaque formation [28]. Lack of sleep therefore greatly decreases glymphatic clearance and can increase Alzheimer's risk in mice. In humans, MRI measurements of infused tracers show that one night without sleep results in a marked decrease of tracer clearance compared to participants who had a normal night's sleep. Glymphatic clearance is therefore decreased in humans with missed sleep. The sleep deprivation group also had a higher concentration of remaining tracer multiple days after the missed night of sleep compared to the control group [29]. This suggests that humans may not make up for lost sleep when considering the impacts of sleep deprivation on glymphatic clearance. These results further suggest sleep may be important to glymphatic waste clearance in both mice and humans.

Respiratory Motion

Respiratory motion may contribute to CSF flow, though experimental results on human and mice are inconclusive. One study using MRI measurements in humans shows that respiratory motion, namely inspiration, contributes to CSF flow to a greater extent than arterial pulsations. Dreha-Kulaczewski *et al.* observed that breath holding suppresses CSF flow while inspirations during forced breathing drive CSF flow, with arterial pulsations minorly contributing to flow [30]. This suggests that breathing is important to CSF flow with inspiration being the driving factor. Studies comparing measurements of the respiratory cycle and CSF flow in mice contradict these findings. Mestre *et al.* found that the root-mean-square fluid velocity peaks from CSF in the periarterial spaces do not correlate with respiration peaks [16], suggesting that respiratory motion does not drive periarterial CSF flow. More work is needed to understand the relationship between respiratory motion and CSF flow.

1.2 Fluid Mechanics

1.2.1 Laminar Flow Between Parallel Plates

This section will consider the mathematical analysis of the viscous flow of a Newtonian fluid between two parallel plates using planar laminae [31]. This provides a simple model for flow in either the artery or periarterial space without considering peristaltic effects.

Laminar flow assumes fluid flow can be treated as an assembly of laminae of uniform thickness and is characteristic of fluids with low Reynolds numbers (see Section 2.1.2) [32]. This derivation will consider unidirectional flow between two parallel plates using the coordinate system and notation pictured in Figure 1.8a. The x direction is defined along the long axis of the channel and is the direction of flow. The y direction is defined along the height of the channel with gravity pointing in the negative y direction. The z direction points along the width of the channel. The x, y, and z velocity components are given by u, v, and w respectively. The half-width of the channel is given by h. In this geometry, the

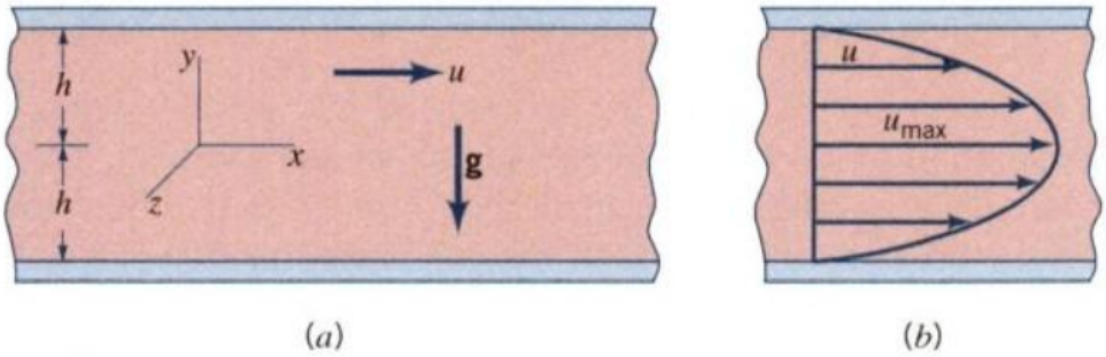

Figure 1.8: Laminar flow between parallel plates. (a) Diagram of coordinates and notation used for analysis. The coordinate system is aligned such that the acceleration due to gravity g points along the negative y axis. The flow in the channel u is orthogonal to gravity. (b) Parabolic velocity profile [31].

width of the channel in the z direction is much larger than the height in y. The aspect ratio and the orientation with respect to gravity defined for this derivation are preserved in the microfluidic channels utilized in this project.

The Navier-Stokes equations satisfying conservation of momentum in the x, y, and z directions are

$$\rho(\frac{\partial u}{\partial t} + u\frac{\partial u}{\partial x} + v\frac{\partial u}{\partial y} + w\frac{\partial u}{\partial z}) = -\frac{\partial p}{\partial x} + \rho g_x + \eta(\frac{\partial^2 u}{\partial x^2} + \frac{\partial^2 u}{\partial y^2} + \frac{\partial^2 u}{\partial z^2}) \tag{1.1}$$

$$\rho(\frac{\partial v}{\partial t} + u\frac{\partial v}{\partial x} + v\frac{\partial v}{\partial y} + w\frac{\partial v}{\partial z}) = -\frac{\partial p}{\partial y} + \rho g_y + \eta(\frac{\partial^2 v}{\partial x^2} + \frac{\partial^2 v}{\partial y^2} + \frac{\partial^2 v}{\partial z^2}) \tag{1.2}$$

$$\rho(\frac{\partial w}{\partial t} + u\frac{\partial w}{\partial x} + v\frac{\partial w}{\partial y} + w\frac{\partial w}{\partial z}) = -\frac{\partial p}{\partial z} + \rho g_z + \eta(\frac{\partial^2 w}{\partial x^2} + \frac{\partial^2 w}{\partial y^2} + \frac{\partial^2 w}{\partial z^2}) \tag{1.3}$$

respectively where ρ is the mass density of the fluid, p is the pressure, and η is the dynamic fluid viscosity. Since flow is unidirectional in the x-direction, it follows that there is no velocity in y and z. From the continuity equation

$$\frac{\partial u}{\partial x} + \frac{\partial v}{\partial y} + \frac{\partial w}{\partial z} = 0, \tag{1.4}$$

it then follows that $\frac{\partial u}{\partial x} = 0$, so u does not vary in the x-direction. Assuming planar laminae, u also does not vary in z; and steady flow implies $\frac{\partial u}{\partial t} = 0$, so u does not vary in time. The velocity u is therefore only a function of y. From these assumptions, the Navier-Stokes equations reduce to

$$0 = -\frac{\partial p}{\partial x} + \eta \frac{\partial^2 u}{\partial y^2} \tag{1.5}$$

$$0 = -\frac{\partial p}{\partial y} + \rho g \tag{1.6}$$

$$0 = -\frac{\partial p}{\partial z} \tag{1.7}$$

acknowledging the orientation of gravity such that $g_x = 0$, $g_y = -g$, and $g_z = 0$ in the given coordinate system.

Integrating equations 1.6 and 1.7 gives

$$p = -\rho g y + f(x) \tag{1.8}$$

which implies there is a hydrostatic pressure in the y direction. Equation 1.5 can be integrated once to give

$$\frac{du}{dy} = \frac{1}{\eta}\frac{\partial p}{\partial x} y + c_1 \tag{1.9}$$

and integrated a second time to give

$$u = \frac{1}{2\eta}\frac{\partial p}{\partial x} y^2 + c_1 y + c_2. \tag{1.10}$$

the constants c_1 and c_2 are dependent on the boundary conditions. For two stationary plates with a no-slip boundary condition, there is no velocity at the plates, or $u = 0$ at $y = \pm h$. Applying the boundary conditions,

$$0 = \frac{1}{2\eta}\frac{\partial p}{\partial x} h^2 \pm c_1 h + c_2 \tag{1.11}$$

which is satisfied if $c_1 = 0$ and

$$c_2 = -\frac{1}{2\eta}\frac{\partial p}{\partial x}h^2. \tag{1.12}$$

Substituting in the constants, the velocity distribution is

$$u = \frac{1}{2\eta}\frac{\partial p}{\partial x}(y^2 - h^2) \tag{1.13}$$

and has the parabolic shape pictured in Figure 1.8b. The maximum velocity occurs in the center of the channel, and velocity decreases as a quadratic function moving toward the plates. We can assume flow in the microfluidic channels used for this project follows this velocity profile at any instant, and this assumption has been confirmed by our results. The velocity of flow in the microfluidic channels varies with time, so the velocity profile also varies in time.

Integrating the velocity u over the height of the channel between the plates and using the equality $-\partial p/\partial x = \Delta p/l$ gives the volume flow rate

$$q = \frac{2h^3\Delta p}{3\eta l} \tag{1.14}$$

where Δp is the pressure drop between an upstream point and a point at distance l downstream with a constant pressure gradient. It is important to note that the volume flow rate q is proportional to the pressure drop Δp. The pressure drop in periarterial spaces is undefined due to the inability to measure it in vivo without changing the flow. Experimental measurements are therefore needed to find the volume flow rates in periarterial spaces. From Equation 1.14, the mean velocity $V = q/2h$ becomes

$$V = \frac{h^2\Delta p}{3\eta l} \tag{1.15}$$

and the maximum velocity, occurring at the center of the channel, can be expressed as

$$u_{max} = \frac{3}{2}V. \tag{1.16}$$

1.2.2 Peristaltic Flow

Peristaltic pumping drives fluid transport through a distensible tube when a wave of area contraction or expansion propagates along its length. Peristalsis is characteristic of all tubular smooth muscle structures, including arteries, as a method for fluid transport [33]. Most studies of peristalsis consider fluid motion in a tube with flexible walls, as is the case in most physiological and industrial contexts. Periarterial flow however occurs in an annulus with a flexible inner boundary and fixed outer boundary. Much less is known about flow in this case. Understanding the extent to which peristalsis can drive fluid flow in an annulus will help elucidate the contribution of arterial pulsations to periarterial CSF flow.

Mathematical Analysis

This mathematical analysis will consider the viscous flow of a incompressible, homogeneous, Newtonian fluid in a two-dimensional channel with one fixed wall and one flexible wall using the coordinate system and notation depicted in Figure 1.9. This provides a model of flow within periarterial spaces while considering a fixed astrocytic endfeet boundary and waves traveling in the flexible arterial wall boundary. Flow through AQP4 channels is not considered in this model. The x and y directions, the corresponding fluid velocity components, and the half-width of the channel are defined similarly to the previous section. A small-amplitude sinusoidal wave travels along the flexible wall with wave speed c, amplitude a, and transverse displacement ζ.

The flow through the channel is governed by the Navier-Stokes equations for the x and y directions and the continuity equation. Introducing the stream function ψ and vorticity ω reduces the governing equations. The stream function solves for the trajectories of particles

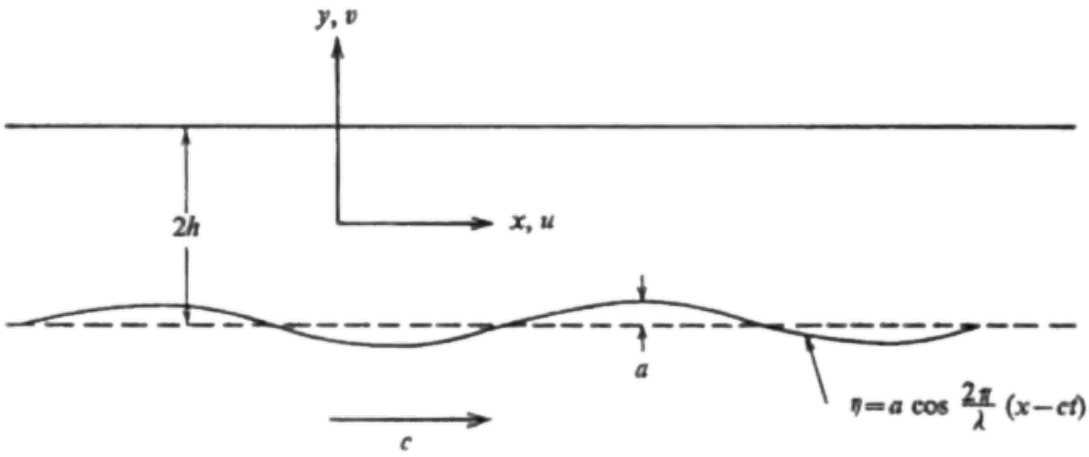

Figure 1.9: Diagram of coordinates and notation used for the mathematical analysis of a two-dimensional channel with one fixed and one flexible wall. A travelling sine wave is imposed on the flexible wall [34].

in a steady flow and is defined in two-dimensions as

$$\frac{\partial \psi}{\partial y} = u \qquad\qquad \frac{\partial \psi}{\partial x} = -v. \tag{1.17}$$

The vorticity solves for the rotation of the fluid and is defined as

$$\omega = \frac{\partial v}{\partial x} - \frac{\partial u}{\partial y}. \tag{1.18}$$

The stream function and vorticity reduce the Navier-Stokes equations to

$$\frac{\partial \psi}{\partial y}\frac{\partial \omega}{\partial x} - \frac{\partial \psi}{\partial x}\frac{\partial \omega}{\partial y} = \nu \nabla^2 \omega \tag{1.19}$$

where ∇^2 is the Laplacian operator and ν is the kinematic viscosity of the fluid [35]. All fluid motion in the channel is dictated by Equation 1.19. In non-dimensional form, the fluid motion is given by

$$\frac{\partial}{\partial t}\nabla^2 \psi + \frac{\partial \psi}{\partial y}\nabla^2 \frac{\partial \psi}{\partial x} - \frac{\partial \psi}{\partial x}\nabla^2 \frac{\partial \psi}{\partial y} = \frac{1}{Re}\nabla^2 \nabla^2 \psi \tag{1.20}$$

where $Re = ch/\nu$ is the Reynolds number [34].

Non-dimensional variables are used for the remaining analysis. The non-dimensional variables are normalized based on h and c and are defined as follows:

$$\tilde{x} = x/h \qquad \tilde{y} = y/h \qquad \tilde{t} = ct/h \qquad \tilde{\psi} = \psi/(ch) \qquad \tilde{\zeta} = \zeta/h. \tag{1.21}$$

The boundary conditions can be written using these nondimensionalized variables. The transverse displacement of the flexible boundary is given by

$$\tilde{\zeta} = \epsilon \cos \alpha(\tilde{x} - \tilde{t}) \tag{1.22}$$

where the amplitude ratio $\epsilon = a/h$ and the wave number $\alpha = 2\pi h/\lambda$. The no-slip boundary conditions at the walls can be written in non-dimensional form as

$$\frac{\partial \tilde{\psi}}{\partial \tilde{y}}\Big|_{\tilde{y}=1} = 0 \qquad\qquad \frac{\partial \tilde{\psi}}{\partial \tilde{x}}\Big|_{\tilde{y}=1} = 0 \tag{1.23}$$

$$\frac{\partial \tilde{\psi}}{\partial \tilde{y}}\Big|_{\tilde{y}=-1-\tilde{\eta}} = 0 \qquad\qquad \frac{\partial \tilde{\psi}}{\partial \tilde{x}}\Big|_{\tilde{y}=-1-\tilde{\eta}} = \alpha\epsilon \sin \alpha(\tilde{x} - \tilde{t}) \tag{1.24}$$

where $\tilde{y} = 1$ describes the height of the fixed top wall and $\tilde{y} = -1 - \tilde{\zeta}$ describes the height of the flexible bottom wall [34].

The governing equation and boundary conditions only depend on the normalized amplitude, wave number, mean flow, and Reynolds number. These equations cannot be solved any further for a general case, but they can be solved by assuming a low Reynolds number and wavelength. This gives a flow with no inertia and an infinite wave, meaning the motion is not periodic. Furthermore, the non-dimensionalized wave number becomes zero, so the streamlines are straight instead of curved. These features describe the Poiseuille flow between parallel plates derived in the previous section.

1.3 Motivation for Study

Understanding CSF flow in periarterial spaces has a range of implications for human health. The following section summarizes current research on human health issues relating to CSF flow and the clearance of brain waste metabolites.

Unhealthy accumulation of multiple metabolic waste proteins in the interstitial space is correlated with and thought to be a cause of neurodegenerative disease [36]. Specifically, amyloid-β and tau protein aggregates are associated with Alzheimer's disease, and α-synuclein aggregates are associated with Parkinson's disease [37]. The glymphatic system is thought to be a key pathway for clearing these wastes and therefore part of the pathophysiology of neurodegenerative diseases. Studies in mice show that 65% of exogenously delivered Aβ is cleared by the glymphatic system [12], suggesting that the glymphatic system is the primary route of Aβ clearance. This is also true of tau [40] and α-synuclein [39] clearance. Understanding how the glymphatic system contributes to neurodegenerative disease pathways can provide insight for preventing and curing neurodegenerative disease.

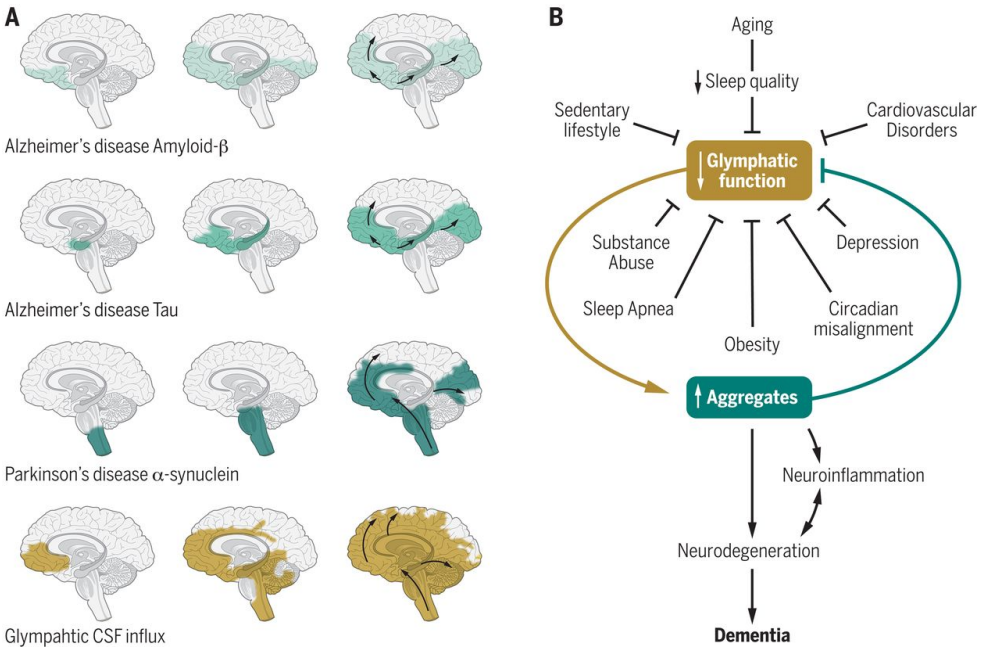

Figure 1.10: The spread of different protein aggregates associated with Alzheimer's disease and Parkinson's disease compared to CSF influx (a) and a proposed role of glymphatic function and protein aggregates in neurodegenerative diseases (b) [37].

Glymphatic function and unhealthy waste protein aggregation go hand-in-hand in mouse models of neurodegenerative disease (Figure 1.11). In APP/PS1 mice, a model of Alzheimer's disease, CSF clearance declines with Aβ accumulation. Injecting Aβ into the CSF of wild-type mice also reduces glymphatic activity [38]. The accumulation of Aβ therefore decreases glymphatic waste clearance. Additionally, CSF influx and clearance are both suppressed in APP/PS1 mice prior to significant Aβ accumulation [38]. Decline in glymphatic function may therefore be both a contributing factor and an early sign of Alzheimer's disease. A decrease in glymphatic activity allows Aβ to accumulate more easily, and accumulated Aβ decreases glymphatic function. This creates a feedback loop of worsening glymphatic function and protein aggregation. A similar feedback loop is found with α-synuclein aggregation in A53T mice, a model of Parkinson's disease [39].

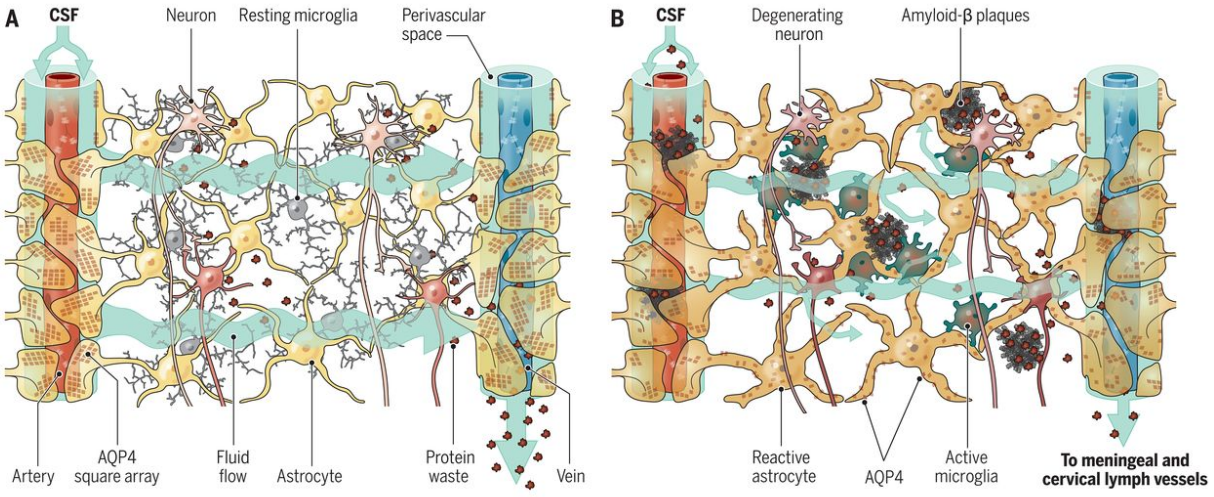

Figure 1.11: Unhealthy protein aggregates negatively impact glymphatic function. a) Diagram of normal waste clearance in healthy glymphatic flow. b) Amyloid-β aggregates block glymphatic flow, which then diminishes waste clearance in a common Alzheimer's disease pathway [37].

This feedback loop may also be involved in tau protein aggregation following traumatic brain injury (TBI). TBI is a known risk factor for early onset of dementia and Alzheimer's disease and has been correlated with an increase in tau protein aggregates. TBI in mice results in a 60% decrease of glymphatic function for at least one month after injury. Tau

proteins are cleared from the brain via glymphatic pathways in mice [40], so reduced glymphatic function after TBI is likely responsible for the increase in tau protein aggregates after TBI.

Age has an impact on glymphatic function, which may explain why neurodegenerative disease is more prevalent in older populations, with old age being the strongest risk factor for developing a neurodegenerative disease [41]. Studies in mice show old age is associated with a rapid decline in glymphatic function and waste metabolite clearance. Clearance of injected Aβ is impaired by 40% in old mice relative to young mice. Additionally, arterial stiffening due old age results in a 27% decrease in arterial wall pulsatility [41]. If arterial pulsations drive CSF flow, then decreasing arterial wall pulsatility could be responsible for impaired glymphatic clearance and increased neurodegenerative disease risk in older populations. Therefore understanding the impacts of arterial pulsations on CSF influx is important for understanding how aging contributes to neurodegenerative disease pathways. Loss of AQP4 polarization in geriatric mice also accompanies a decline in CSF-ISF interchange [41]. Understanding the role that AQP4 channels play in CSF and ISF transport can clarify how this contributes to the connection between aging and neurodegenerative disease risk.

CSF also plays an important role in acute ischemic stroke. An ischemic stroke occurs when a cerebral artery is blocked, which prevents the circulation of blood, oxygen, and glucose to the brain. MR studies in mice found that CSF flows rapidly into periarterial spaces within minutes of occlusion and coincides with tissue swelling and increased water content [42]. It is therefore likely that CSF influx is the driving factor in acute tissue swelling following ischemic stroke. Understanding the mechanisms of CSF flow could elucidate the pathway of rapid CSF influx and resultant tissue swelling after ischemic stroke.

Chapter 2

Methods

2.1 Microfluidics

2.1.1 Device Design and Fabrication

The microfluidic devices used in this study have two stacked channels with a thin membrane separating them (Figure 2.1). The two channels mimic the inner artery and periarterial space while the thin membrane mimics the flexible arterial wall. Fluid is pumped through one channel with a peristaltic pump while the resulting flow of a polystyrene bead suspension is observed in the other channel. These devices are adapted from designs by Keelin Quirk MHC '20 [43].

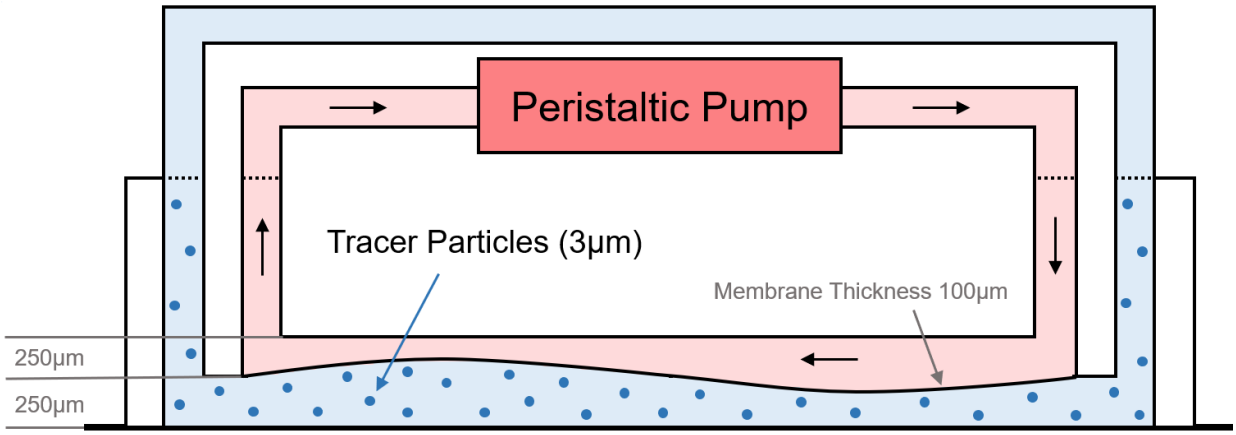

Figure 2.1: Side view diagram of the microfluidic device. The two channels are both 250 μm high and are separated by a flexible, 100 μm thick, PDMS membrane. Water is pumped through the top channel using a peristaltic pump. The flexible membrane moves in response, which then influences the motion of a suspension of 2.789 μm diameter tracer particles in the lower channel.

The devices are built by vertically stacking layers of polydimethylsiloxane (PDMS) onto a glass coverslip (Figure 2.2). The footprint of the device is 12 mm wide and 24 mm long.

From bottom to top, the device is made of the glass coverslip, lower channel, gasket, upper channel, and thick PDMS top. The upper and lower channels are both 1 mm wide and 250 μm tall. The lower channel is 16 mm long, while the upper channel is 10 mm long. The tubing holes are 1.3 mm diameter in the gasket and upper channel layers and 1.5 mm diameter in the PDMS top. This allows for pressure-fitting of the tubing in the device. These dimensions have been slightly altered from Quirk's original design to improve the alignment between the layers.

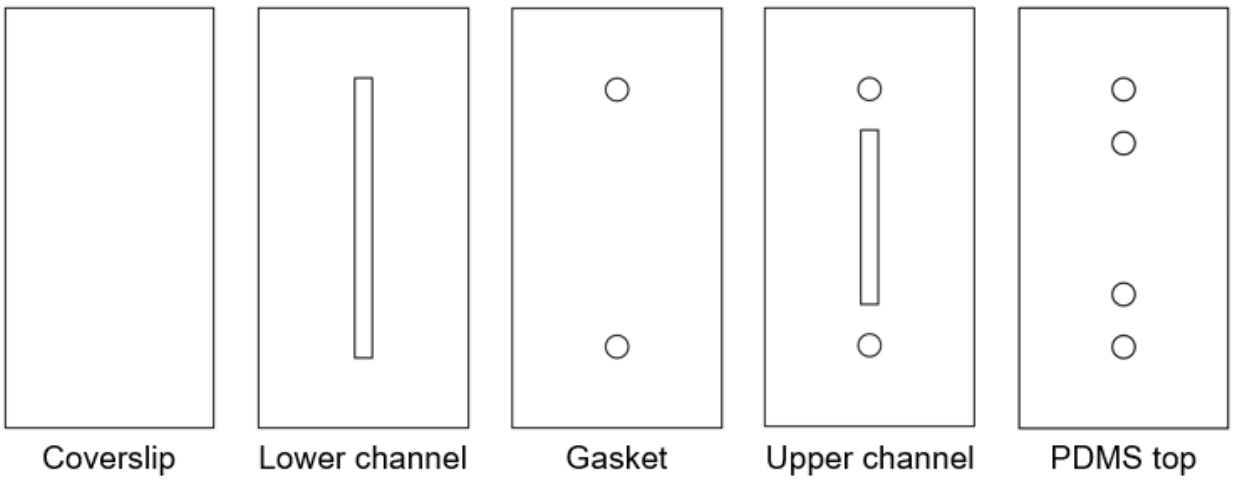

Figure 2.2: Layers of the microfluidic devices in order from the bottom coverslip on the left to the PDMS top on the right. The footprint of each layer is 12 mm wide and 24 mm long. The channels are 1 mm wide for both the lower and upper channels. The lower channel is 16 mm long while the upper channel is 10 mm long. The tubing holes are 1.3 mm in diameter for the gasket and upper channel layers and 1.50 mm in diameter for the PDMS top.

PDMS is commonly used in microfluidic manufacturing due to its tunable rigidity when mixing the two-part elastomer and curing agent. The devices used are built using a combination of pre-manufactured SiMPore ultra-thin PDMS sheets and PDMS mixed in the lab from a Sylgard 184 silicone elastomer kit. The lower channel and upper channel layers are cut from 250 μm SiMPore PDMS sheets while the gasket layer is cut from a 100 μm SiMPore PDMS sheet. Quirk's design used 300 μm SiMPore PDMS sheets for the lower channel and upper channel layers, however the 300 μm thick PDMS sheets were not available at the time of building these devices. A Cricut craft cutter is used for precision cutting of the channel

and tubing-hole details of these three layers. The PDMS top is prepared from 10:1 Sylgard 184 and varies in thickness from 3 to 3.5 mm. A 1.5 mm diameter circular punch is used to make the tubing holes in the PDMS top.

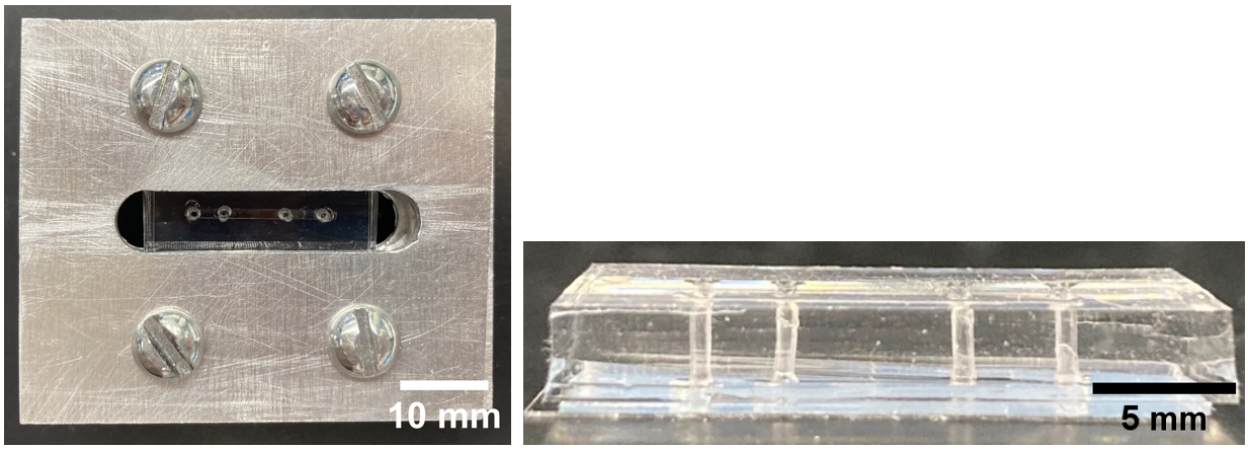

Figure 2.3: Constructed microfluidic device. Left: Top view of a device held together in a metal clamp. Right: Side view of a device with the clamp removed.

The device is assembled by first dragging the lower channel layer onto a cut glass coverslip with angled reverse tweezers. The lower channel layer is cleaned with Scotch tape immediately before assembling, as is the case for all following layers, and gloves are worn during assembly to prevent oils from accumulating on the PDMS. These measures improve the PDMS-glass and PDMS-PDMS adhesion. The gasket layer is dragged on next with a few drops of isopropanol between the gasket and lower channel layers. The isopropanol allows for slippage between the layers, which makes adjusting the alignment easier. The upper layer is dragged on following in a similar fashion. The device is then placed in a vacuum oven at 80°C and 50 cmHg to help the isopropanol evaporate out of the device and remove air bubbles. The remaining isopropanol and air bubbles are pushed out of the device by tapping it with tweezers. The PDMS top is aligned on top and the completed device is placed in a metal clamp (Figure 2.3). The clamp holds the device together sufficiently to maintain separation between the channels. The clamp is used as a substitute for binding, which is an intensive process involving multiple iterations of oxygen-plasma cleaning.

After a set of experiments, the devices cannot be reused in their assembled state due to polystyrene beads drying into the lower channel. However, some parts of the devices can be separated, cleaned, and reassembled into a new device. The PDMS top and upper channel layers do not require special cleaning before reuse since they are only in contact with water in the upper channel. The gasket and lower channel layers can be cleaned with isopropanol to remove dried beads before reassembling. These layers can only be recycled a few times the before residual dried beads accumulate noticeably. The glass coverslip is best replaced for each reassembly.

2.1.2 Device Parameters

Several parameters describing the fluid motion in the microfluidic device can be extracted from the governing equations of motion. We can use these parameters to compare how our microfluidic experiments compare to both in vivo measurements in periarterial spaces and previous measurements using similar microfluidic devices.

Overview of Parameters

The Reynolds number is a ratio of inertial and viscous forces and determines whether flow is laminar or turbulent. A small Reynolds number implies laminar flow, where streamlines flow parallel to one another, while a large Reynolds number implies turbulent flow, where streamlines cross and curl into eddies (Figure 2.4). Laminar flows are characterized by minimal mixing between laminae with diffusive effects dominating mixing between streams. The Reynolds number Re for flow of a fluid through a channel is calculated as

$$Re = \frac{V * l}{\nu} \tag{2.1}$$

where V is the fluid velocity, l is the characteristic length of the channel, and ν is the kinematic viscosity of the fluid. Reynolds numbers less than 2300 generally indicate laminar

flow while Reynolds numbers greater than 2300 generally indicate turbulent flow [44]. The Reynolds number for the transition between laminar and turbulent regimes is typically on the order of magnitude of 10^3, though the exact Reynolds number for this transition is dependent on the system. Within the laminar regime, Reynolds numbers below 1 indicate Stokes flow, where the velocity profile is parabolic (see Section 1.2.1).

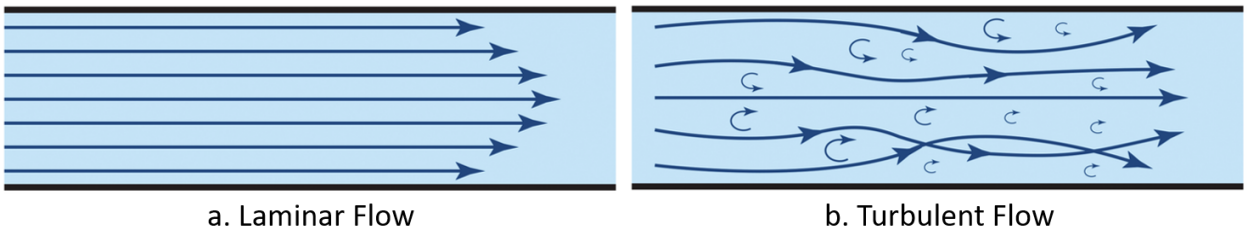

Figure 2.4: Diagram of streamlines for (a) laminar and (b) turbulent flow in a pipe. Streamlines in laminar flow run parallel to each other. Turbulent streamlines cross and curl into eddies [46].

The Péclet number describes the extent to which solute transport in a fluid flow is diffusive or advective. Diffusive or Brownian motion is dictated by solutes taking random walks through the solvent as they spread into areas of lower solute concentration. Advection is the transport of solutes driven by the solvent fluid velocity. Higher Péclet numbers indicate solutes are moved primarily through advection while lower Péclet numbers indicate solutes are moved primarily through diffusion. The Péclet number Pe is given by

$$Pe = \frac{V * l}{D} \tag{2.2}$$

where D is the diffusion coefficient. For diffusion of uniform spherical particles through a low Reynolds number fluid, the diffusion coefficient can be calculated using the Stokes-Einstein equation

$$D = \frac{k_B T}{6\pi\nu\rho r} \tag{2.3}$$

where k_B is the Boltzmann constant, T is the temperature, ν is the kinematic viscosity of the fluid, ρ is the mass density of the fluid, and r is the radius of the spherical particles [16].

Péclet numbers below 1 generally idicate that diffusion dominates while Péclet numbers above 1 generally indicate that advection dominates.

Parameters Calculated for This Experiment

For these calculations, we used the kinematic viscosity of water at 20°C. The viscosity of CSF is similar to viscosity of distilled water [45], so CSF is modeled well by water. The velocity used is an average over multiple experiments using pumping frequencies from 1-3 Hz, and the hydraulic diameter of the microfluidic channel was used for the characteristic length. The hydraulic diameter D_h of any channel geometry is defined as

$$D_h = \frac{4 * cross\text{–}sectional\ area\ of\ flow}{wetted\ perimeter\ of\ channel}\ [47], \tag{2.4}$$

and for a rectangular channel with cross-sectional width b and height h, the hydraulic diameter is given by

$$D_h = \frac{4bh}{2b + 2c} = \frac{2bh}{b + h}. \tag{2.5}$$

For rectangular microfluidic device channels that are 250 μm tall and 1 mm wide, the hydraulic diameter is 4 x 10^{-4} m. We calculated a Reynolds number of 0.0717 for this experiment, meaning flow within the device follows Stokes flow, and a Péclet number of 4.65 x 10^5, meaning advective transport of particles dominates over diffusion. A summary of the chosen and calculated parameters can be found in Table 2.1.

Parameters	Current experiment
ν [m^2/s]	1.00 x 10^{-6}
V [m/s]	1.79 x 10^{-4}
l [m]	4.00 x 10^{-4}
D [m^2/s]	1.543 x 10^{-13}
Re	0.0717
Pe	4.65 x 10^5

Table 2.1: Parameters chosen and calculated for this experiment.

Comparison with In Vivo Experiments and Previous Microfluidic Experiments

The parameters calculated in the previous section can be compared to those calculated for experiments in live mice and for previous experiments using similar microfluidic devices. Experiments in live mice by Mestre et al. tracked the flow of 1 μm diameter particles through periarterial spaces. For their calculations, they used measurements of the spatial mean of the time-averaged velocity for V and measurements of the average periarterial space width for the characteristic length (Figure 2.5a-b). They additionally used the kinematic viscosity of water at 38.6°C and a diffusion coefficient calculated for 1 μm spherical particles to calculate values of the Reynolds number and Péclet number (Figure 2.5c-d).

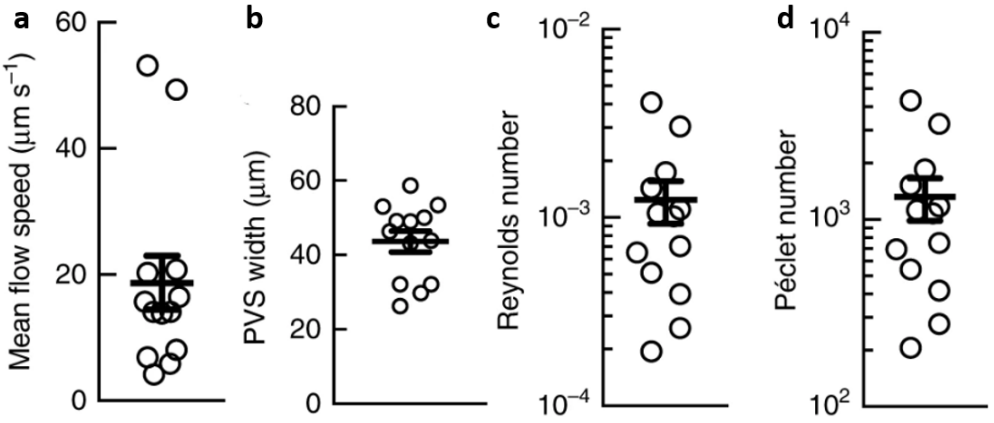

Figure 2.5: Parameters for periarterial spaces in mouse brains measured by Mestre el at. (a) Time-averaged mean flow speeds measured. (b) Average measurements of the periarterial space width. (c) Reynolds number and (d) Péclet number calculated using the experimental mean flow speed and periarterial width measurements [16].

Previous experiments by Quirk [43] used similar microfluidic devices and methods to this experiment. Similar to our calculations, Quirk used the kinematic viscosity of water at 20°C and used the hydraulic diameter of the rectangular microfluidic channel for the characteristic length. For the velocity, Quirk used a measurement of the mean flow speed in the microfluidic device with a peristaltic pumping frequency of 1 Hz. A comparison of all chosen and calculated parameters for the three experiments is summarized in Table 2.2

The Reynolds numbers for all three experiments indicate that the flow regime is laminar. The high aspect ratio of the microfluidic channel and orientation with respect to gravity will

Parameters	Mestre et al. [16]	Quirk [43]	Current experiment
ν [m^2/s]	0.697 x 10^{-6}	1.00 x 10^{-6}	1.00 x 10^{-6}
V [m/s]	approximately 10^{-5}	2.0 x 10^{-5}	1.79 x 10^{-4}
l [m]	4.4 x 10^{-5}	4.61 x 10^{-5}	4.00 x 10^{-4}
D [m^2/s]	6.55 x 10^{-13}	4.039 x 10^{-13}	1.543 x 10^{-13}
Re	approximately 10^{-3}	9 x 10^{-3}	0.0717
Pe	approximately 10^3	2.3 x 10^4	4.65 x 10^5

Table 2.2: Comparison of parameter values chosen and calculated between in vivo experiments from Mestre et al., previous microfluidic experiments by Quirk, and this experiment.

allow us to consider this laminar flow as having a velocity profile derived from Poiseuille flow at any instant (see Section 1.2.1). The Péclet number for this experiment is one order of magnitude greater than calculated by Quirk and two orders of magnitude larger than calculated by Mestre et al. This is impacted both by the flow velocities in this experiment being one order of magnitude larger than in the other experiments and by the smaller particles used by Mestre et al. Since this experiment is interested in observing the advective transport of particles, having a larger Péclet number is not an issue.

2.2 Preliminary Work

2.2.1 Rigidity Calculations

Previous experiments by Quirk [43] pumped water through the lower channel of the microfluidic device and observed the flow of a polystyrene bead suspension in the upper channel. The device is imaged from below, so one must image through the glass coverslip, a 250 μm tall channel of water, and a 100 μm thick PDMS sheet before reaching the bottom of the bead suspension in this arrangement. A more optically efficient arrangement is to swap the channels – pump water through the upper channel and observe the bead suspension in the lower channel. Measurements in these two arrangements are comparable if the boundary conditions in the two channels are similar.

We used the rigidity of the channel boundaries as a comparison for the boundary conditions. The flexural rigidity of a thin plate with thickness h is given by

$$D = \frac{Eh^3}{12(1-\sigma^2)} \tag{2.6}$$

where E is the Young's modulus and σ is the stress [48]. For these calculations, we are most concerned with the relationship between the elastic modulus and the thickness. The elastic modulus is inherent to the material while the thickness depends on the geometry. Increasing the elastic modulus can increase rigidity, such as how a sheet of glass is much stiffer than a sheet of paper of the same thickness. Similarly, increasing the thickness can increase rigidity, such as how a thick stack of paper is much stiffer than a single sheet.

Both channels share a boundary of the 100 μm thick PDMS gasket layer, so only the two outside boundaries need to be considered. The upper channel is bounded by the 3 mm-thick PDMS top from above, and the lower channel is bounded by a glass coverslip from below. The PDMS top has a thickness of 3 mm and an elastic modulus of 3 MPa [49]. The borosilicate glass coverslip has a thickness of about 170 μm and an elastic modulus of 64 GPa [50]. Assuming equivalent shear stress on the two boundaries, the ratio of flexural rigidities between the PDMS top and glass coverslip is 0.26. This means that the glass coverslip is about four times as rigid as the PDMS top. This difference is small enough to consider the boundaries similar and proceed with using the lower channel for the induced flow while actively pumping fluid in the upper channel.

2.2.2 Peristaltic Pump Parameters

Water was actively pumped through the upper channel of the microfluidic device using a peristaltic pump. Peristaltic pumps drive fluid flow by compressing a section of tubing with a series of rotating rollers. A Longer Pump BT100-3J peristaltic pump fitted with a Longer Pump DG-1-B/D pump head was used. The frequency in hertz of pumping is dependent on

the rotations per minute of the pump head and the number of rollers in the pump head as

$$frequency\ in\ hertz = \frac{number\ of\ rollers}{60} * rpm. \tag{2.7}$$

This relationship was confirmed experimentally using a 4-roller Longer Pump BQ50-1J peristaltic pump (Figure 2.6). The combination of the Longer Pump BT100-3J peristaltic pump, with a range of 0.1 to 100 rpm, and the 10-roller Longer Pump DG-1-B/D pump head provide a possible pumping frequency range of 0.0167 to 16.67 Hz. In comparison, the Longer Pump BQ50-1J peristaltic pump used in previous experiments by Quirk [43] has a range of 1 to 50 rpm and a 4-roller head, limiting it to a frequency range of 0.067 to 3.33 Hz. The new peristaltic pump acquired for this project greatly broadens the range of pumping frequencies that can be tested.

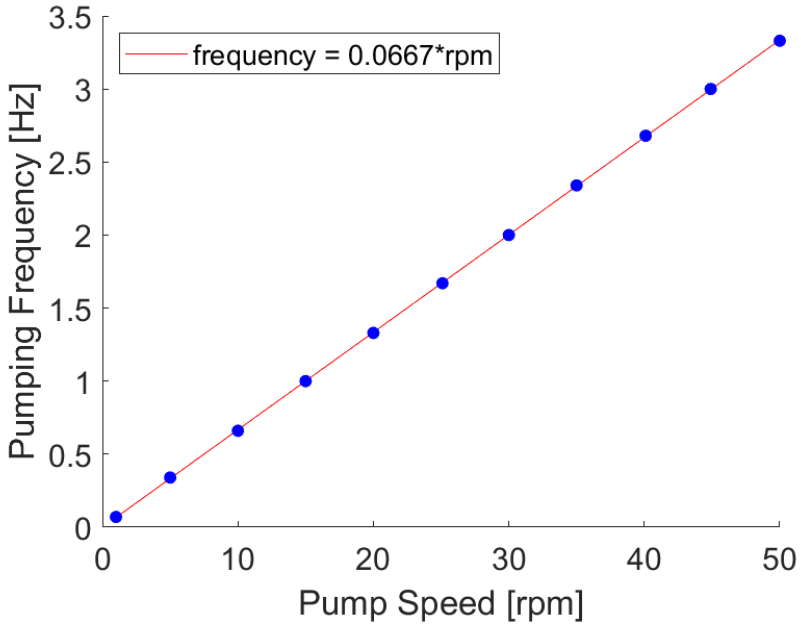

Figure 2.6: Pumping frequencies vs. pump head rotational speed tested on a Longer Pump BQ50-1J with a 4-roller head. The slope of the linear trendline equates to four rollers divided by sixty seconds, confirming the relationship in Equation 2.7.

2.2.3 Microsphere Settling

The positions of 2.789 μm diameter polystyrene beads diluted in water were used to measure fluid motion within the microfluidic device. Measurements rely on the polystyrene beads being evenly suspended through the height of the channel. Polystyrene has a density of 1060 kg/m^3 while water has a density of 997.77 kg/m^3. The greater density of polystyrene results in the beads sinking in water from the hydrostatic pressure. Due to counteracting buoyant forces, the polystyrene beads accelerate downward until they reach a terminal velocity. Once the the beads accelerate to the terminal velocity, they will continue falling at the terminal velocity until they reach the bottom of the channel. Determining the terminal velocity at which the beads sink in the channel is important to ensure the assumption of suspended beads holds over the duration of flow measurements.

The terminal velocity of polystyrene beads sinking in water is determined by the Stokes settling speed. The Stokes settling speed for a solid sphere in a fluid is given by

$$v = \frac{2}{9}\frac{(\rho_p - \rho_f)}{\eta} g R^2 \tag{2.8}$$

where ρ_p is the mass density of the spherical particle, ρ_f is the mass density of the fluid, η is the dynamic fluid viscosity, g is the acceleration due to gravity, and R is the radius of the spherical particle [51].

The Stokes settling speed for the particles used is 0.2964 μm/s. In a 250 μm high channel, this results in a settling time of 14.06 minutes. All videos captured in the project are 45 seconds long, so the settling time is inconsequential within each video. However, the bead suspension needed to be vortexed and recycled right before each video capture to ensure the even suspension of particles at the start of the video.

2.2.4 Camera Calibration

We calibrated the size of pixels in our images to obtain distance measurements within the microfluidic device. The correlation between pixels and physical distance needed to be measured for the particular combination of camera and microscope objective used. We took an image of a micrometer slide with the desired setup and used ImageJ to measure the length in pixels of know distances on the micrometer. We measured multiple lengths of 0.05 mm on a micrometer (Figure 2.7). The average of these measurements gave a conversion factor of 0.000658 mm per pixel.

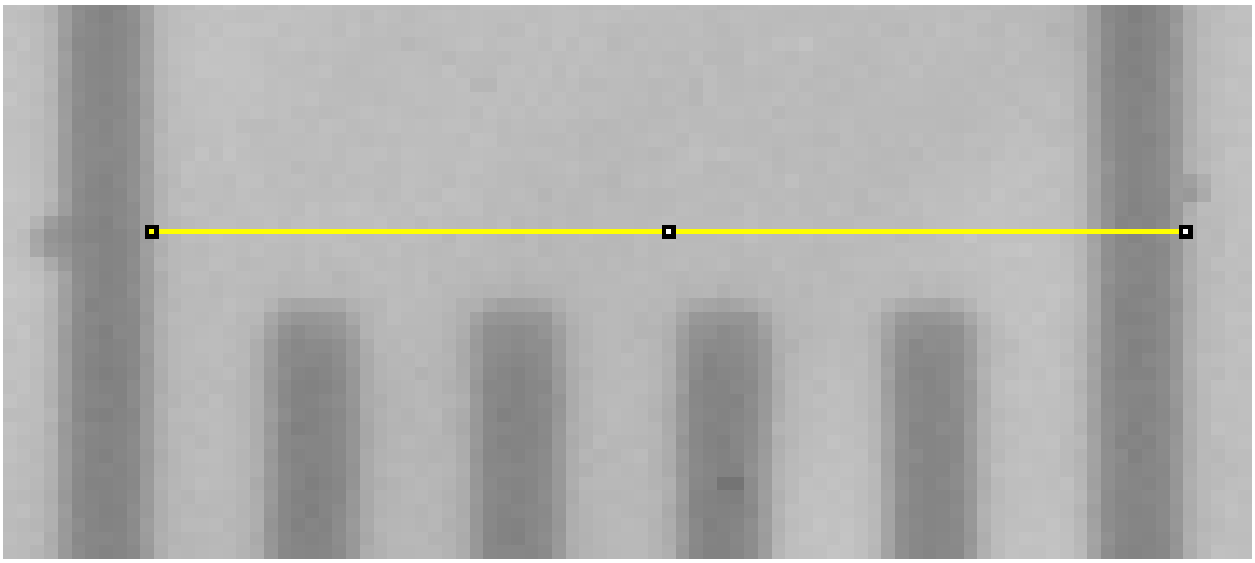

Figure 2.7: Example of a measurement of 0.05 mm on a micrometer using ImageJ.

2.3 Experimental Methods

2.3.1 Capturing Motion Within the Microfluidic Device

Measuring motion within the microfluidic device requires recording high speed video of a suspension of polystyrene microspheres in the lower channel under a microscope. A Phantom v1611 high speed camera was mounted onto a Nikon Eclipse TS100 microscope. All video was taken using brightfield microscopy at 1000 fps and using a Nikon LWD 40x Ph1 ADL ∞/1.2 Phase Contrast microscope objective.

At the maximum camera resolution possible using this setup, the videos captured show a central circular region of video through the microscope with surrounding "dead" space. At this maximal resolution, 1000 fps videos are limited to 16.541 seconds due to storage limitations inherent to the camera. In order to maximize the time of continuous data collection, videos were taken using a 768 x 480 resolution, which captured most of the central region while minimizing the dead space captured. At this resolution, 1000 fps videos were captured for the maximum time of 45.789 seconds. The longer data collection time improves the statistics of velocity measurements within the device. In contrast, previous work by Quirk [43] used videos around 16 seconds in length and combined three consecutive videos for each pumping frequency tested. While this can improve the statistics, it is limited by the discontinuity of particle tracks between videos and the lag time between videos from offloading the camera data.

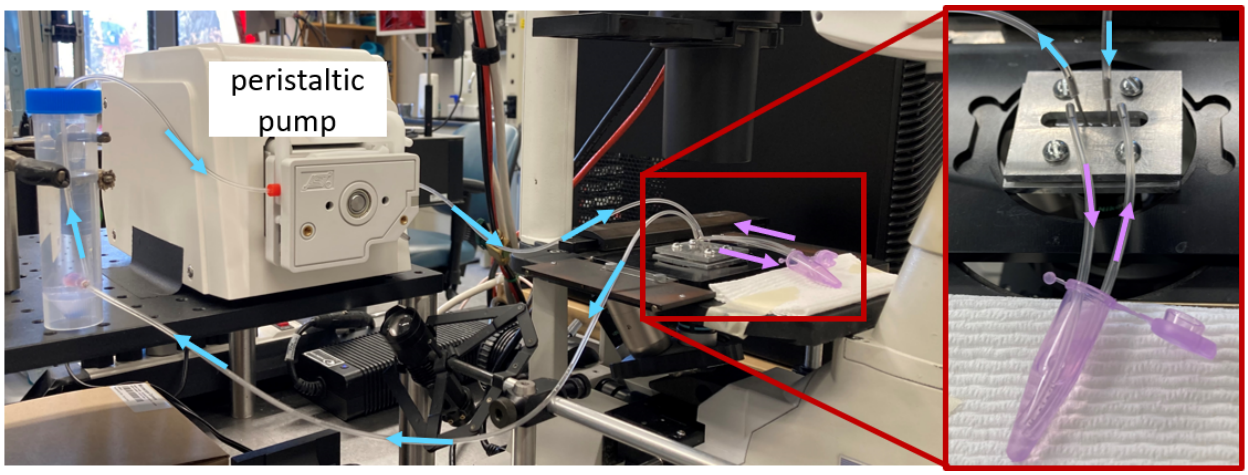

Figure 2.8: Circulation of flow. Flow of water through the upper channel (blue arrows) is pumped by the peristaltic pump and recycled through an air trap. Flow of the bead suspension through the lower channel (purple arrows) is recirculated using a microcentrifuge tube. Red box: closer view of the two flows through the device.

Water is pumped through the upper channel by a Longer BT100-3J peristaltic pump fitted with a Longer DG-1-B/D pump head and using and 1/32 inch ID vinyl tubing (Figure 2.8). The peristaltic pump is placed at a similar height to the microfluidic device on the microscope stage to minimize changes in elevation, and therefore minimize changes in the

hydrostatic pressure of the circulating water. The tubing is cut to a minimal length while maintaining enough flexibility for assembling and disassembling the setup. After exiting the upper channel, the water circulates through an air trap before traveling back through the peristaltic pump. The air trap is made by a 50 mL centrifuge tube with tubing entering near the bottom and exiting through the cap. The tube is only partially filled with water to leave a region of air at the top. The tubing fills with air between experiments, which affects flow. When those air pockets are pushed into the air trap by water pumping through the tubing, they travel up the centrifuge tube as air bubbles and exit the circulating fluid.

The lower channel is filled with a 130x dilution of 2.789 μm Polysciences Dyed Violet Microparticles in water. The same 1/32 inch ID vinyl tubing as before is used for recirculation via a microcentrifuge tube reservoir. A 25 mL stock of the bead suspension was prepared on each day of experiments. Before each video capture, the stock suspension was vortexed, and the lower channel was filled with the vortexed stock using a pipette. This helps limit the effects of particle settling between experiments (see Section 2.2.3).

2.3.2 Considerations for Field of View

For these experiments, it is important to consider the region within the lower microfluidic channel filmed in regards to the distance between the two ends of the channel, the height within the channel, and the distance from the side walls.

The lower channel of the device is 16 mm long with the tubing diameter covering 1.5 mm on each end, allowing for a middle 13 mm region of unobstructed flow. Similarly, the upper channel is 10 mm long with the tubing diameter covering 1.5 mm on each end, allowing for a middle 7 mm region of unobstructed flow. For these experiments, we are interested in the region of the lower channel where waves in the membrane can induce flow. The two channels are centered on top of each other, so flow is best observed in the middle 7 mm region of the lower channel. For videos taken at a 768 x 480 pixel resolution and a pixel size of 0.000658 mm, the width of the videos is 0.505 mm or 7.2% of the length of this 7 mm

optimal length regime. We took videos near the center of the channel length to capture this region of induced flow while minimizing effects of the tubing at the far ends.

Flow within the microfluidic channel is laminar along the long rectangular channel with parallel top and bottom walls. Without considering motion of the top boundary, we can compare flow within the channel to Poiseuille flow. Poiseuille flow has a parabolic velocity profile as height varies in the channel such that the maximum velocity occurs at the mid-height of the channel and the velocity goes to zero at the top and bottom walls (see Section 1.2.1). The parabolic velocity profile also gives that the change in velocity with height is smallest near the mid-height and largest near the top and bottom walls. Therefore, the velocity is similar to the maximum velocity at heights near the mid-height. For this experiment, video was taken with the microscope focused on the mid-height of the channel to capture the maximum velocity. In a 250 μm tall channel, velocities within 10% of the maximum are expected at heights within 40 μm of the mid-height.

Previous experiments by Quirk [43] quantified flow behavior near the side walls of the microfluidic channels. They found that the velocity profile along the width of the channel was flat for 30% of the total channel width when using a pumping frequency of 1 Hz and for 60% of the total channel width when using pumping frequencies of 2 and 3 Hz. For the 1 mm wide microfluidic channel imaged at a 768 x 480 pixel resolution with a pixel size of 0.000658 mm, the width of the channels captured is 0.316 mm or 31.6% of the total channel width. Therefore, when imaging at the mid-width and mid-height of the channel, the field of view should capture a region with uniform particle velocities along the vertical axis of the video frames.

2.3.3 Membrane Waveform Approximation

Peristaltic pumping drives fluid motion in a closed tube by compressing a stationary section of the tubing with a rotating head of rollers. The compression propagates an elastic wave through the tubing at a speed on the order of the speed of sound. The speed of

sound through PDMS is on the order of 10^3 m/s, ranging from 1020 m/s to 1060 m/s for Sylgard 184 [53], while instantaneous velocities measured in the microfluidic channel are on the order of 10^{-3} m/s. Since the speed of sound in PDMS is many orders greater than the speed of motion in the microfluidic channel, we can assume the waveform of the membrane motion between the microfluidic device channels is coincident with the waveform of the tubing compressed by the pump head rollers. Simultaneous measurement of the peristaltic pump head motion and motion within the microfluidic device therefore can provide insight into the relationship between pumping motion and driven fluid flow.

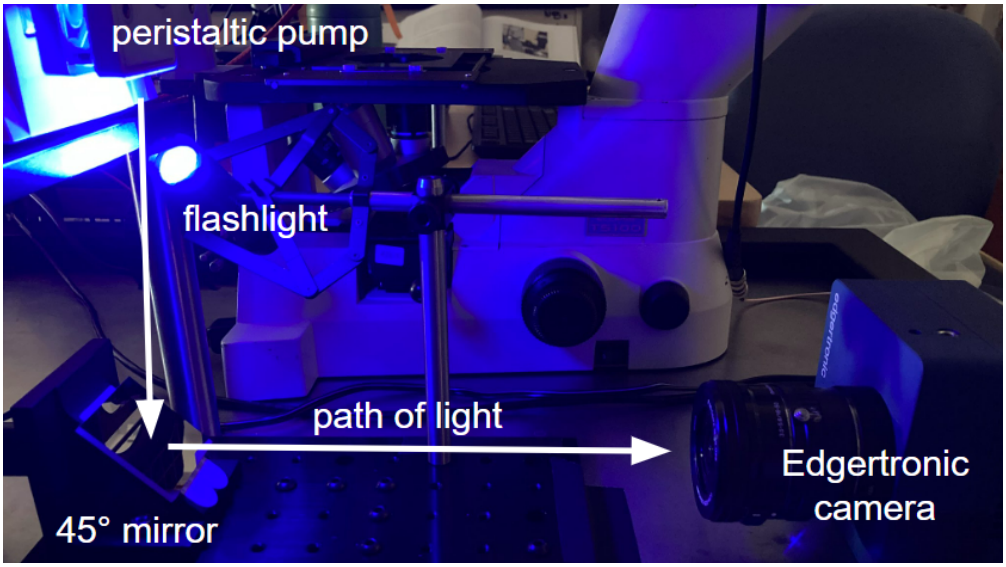

Figure 2.9: Capturing the position of rollers in the peristaltic pump head.

The Longer Pump DG-1-B/D Peristaltic Pump Head used has ten evenly spaced rollers. When in use, the tubing is stretched on top of the ring of rollers and is maximally compressed when a roller is positioned at the center top of the ring. The rollers are most visible from below the pump head, where the roller positions mirror the rollers on the top half of the pump head. Due to this symmetry, the position of rollers passing through the center bottom of the ring directly corresponds to the position of rollers passing through the center top of the ring.

An Edgertronic SC1 camera with a Sony E PZ 16–50 mm F3.5–5.6 OSS APS-C Wide-angle Power Zoom Lens was used capture the motion of rollers on the peristaltic pump (Figure 2.9). The Edgertronic camera and the Phantom v1611 camera were both connected to an external trigger to ensure simultaneous video capture. A mirror was angled at 45 degrees from vertical to view the pump head rollers from below. A flashlight was positioned to illuminate the rollers. Video was captured at a frame rate of 200 fps.

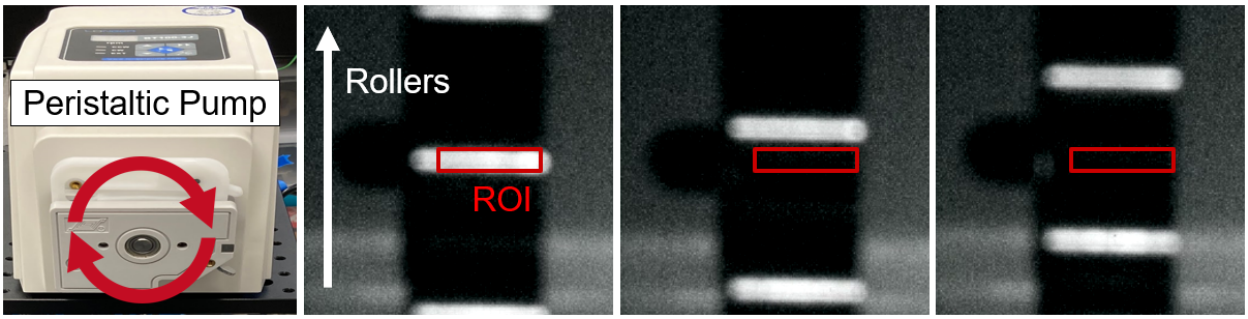

Figure 2.10: Measuring the phase of the peristaltic pump head rollers. Left image: The rollers in the pump head turn clockwise. Right three images: The rollers appear as bright bars in the video capture. A region of interest (red rectangle) is selected at the center bottom of the pump head. As time progresses from left to right, the brightness within the region of interest is averaged for each frame.

The waveform was approximated by measuring brightness at the center bottom of the pump head (Figure 2.10). The rollers appear as bright bars against a dark background in the video capture. Measuring pixel brightness at the center bottom of the pump head therefore gives the waveform of tubing compression. A region of interest was selected in the video corresponding to the center bottom of the pump head. The pixel brightnesses were averaged in this region for each frame. This produced a boxy sine wave corresponding to the tubing compression by the pump rollers (Figure 2.11). This wave was used as an approximation for the membrane waveform between the microfluidic channels.

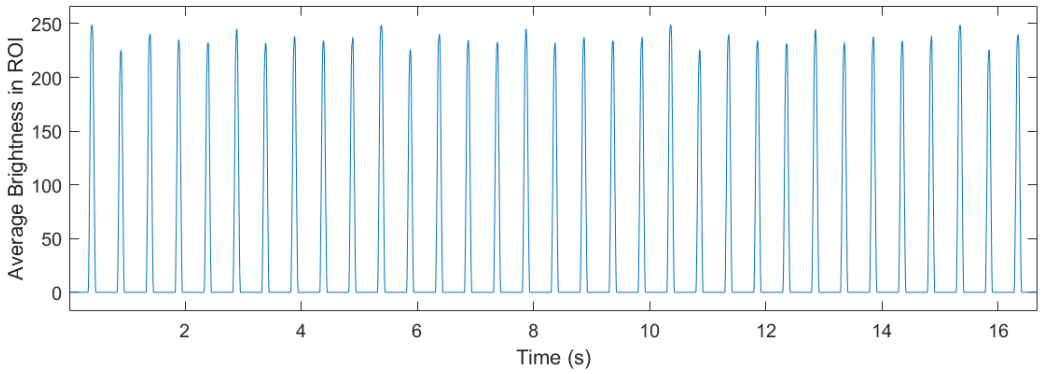

Figure 2.11: Example waveform approximation measured from the pump head rollers. The waveform was extracted by averaging the brightness in a region of interest for each frame.

2.4 Analysis Methods

2.4.1 Particle Tracking

This experiment used a 2D particle tracking method developed by John Crocker and Eric Weeks [52]. The particle tracking algorithm was originally written in IDL and was later translated into MATLAB with some limitations. The code first prepares frames through a series of image processing steps. The frames are flipped right to left so that the direction of pumped flow appears left to right, and so displacements along the direction of pumping are calculated as positive values. An average background image is calculated and subtracted, the frames are inverted so the particles appear bright against a dark background, and the frames are bandpassed and tresholded to feature the desired particles (Figure 2.12). The code then identifies the centroid of each featured particle and makes a list of the centroid positions in each frame. A tracking function is run on the centroid list, which strings together centroid positions between frames into continuous tracks using combinatorics based on parameters for the maximum displacement between frames, the minimum length of a track in frames, and the maximum gap in frames for which two centroid positions can be connected into a track.

The 2D tracking algorithm used has limited capability for tracking fast moving samples. This becomes an issue for tracking videos with a pumping frequency above 3 Hz. Data was

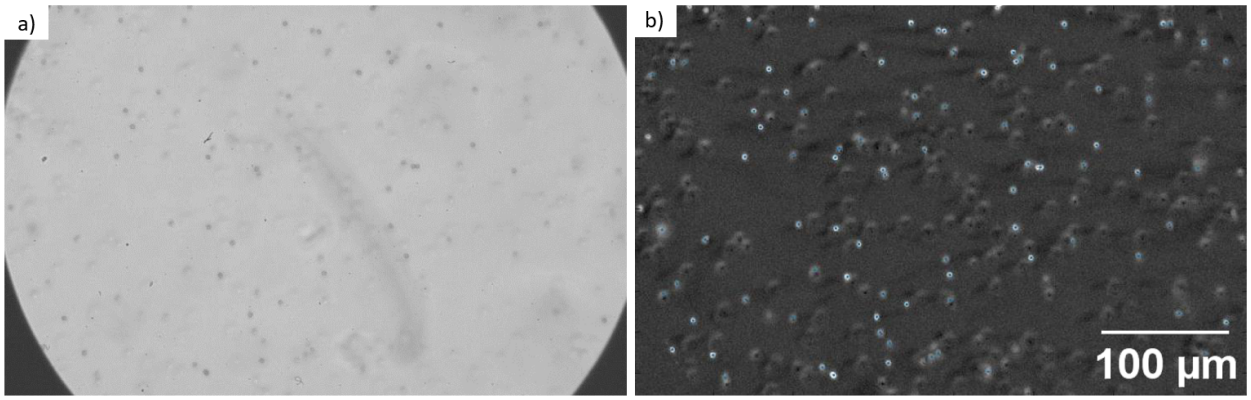

Figure 2.12: Image processing steps are used to feature particles before identifying and tracking the particle centroids. (a) Raw brightfield frame. (b) Corresponding frame inverted with the average background removed. The white circles are featured particles, and the blue dots are identified centroids. Both images are at the same scale.

collected for this project with pumping frequencies between 1 and 12 Hz in an effort to broaden the frequency range previously tested by Quirk. This frequency range also has the benefit of capturing frequencies corresponding to human heart rates (1-3 Hz), rat heart rates (4-8.33 Hz), and mouse heart rates (8.33-11.67 Hz). Predictive tracking, originally developed by Ouellette, is better suited for tracking data at these frequencies where the maximum displacement between frames overloads the combinatorics used by 2D tracking. A version of predictive tracking will need to be adapted to analyze this data.

Chapter 3

Results

3.1 Induced Flow Motion Over Time

3.1.1 Velocity Distributions

Velocity distributions are generated by combining instantaneous velocity measurements in the direction along the length of the microfluidic channel from multiple datasets. Combining multiple datasets increases the statistical significance of the information provided by the velocity distribution. Velocity distributions for pumping frequencies from 1-3 Hz are shown in Figure 3.1. Distributions combine three experiments except for 1 Hz and 2.33 Hz combining two experiments and 2.67 Hz displaying one experiment. Positive velocities correspond to motion in the direction of pumping in the upper channel.

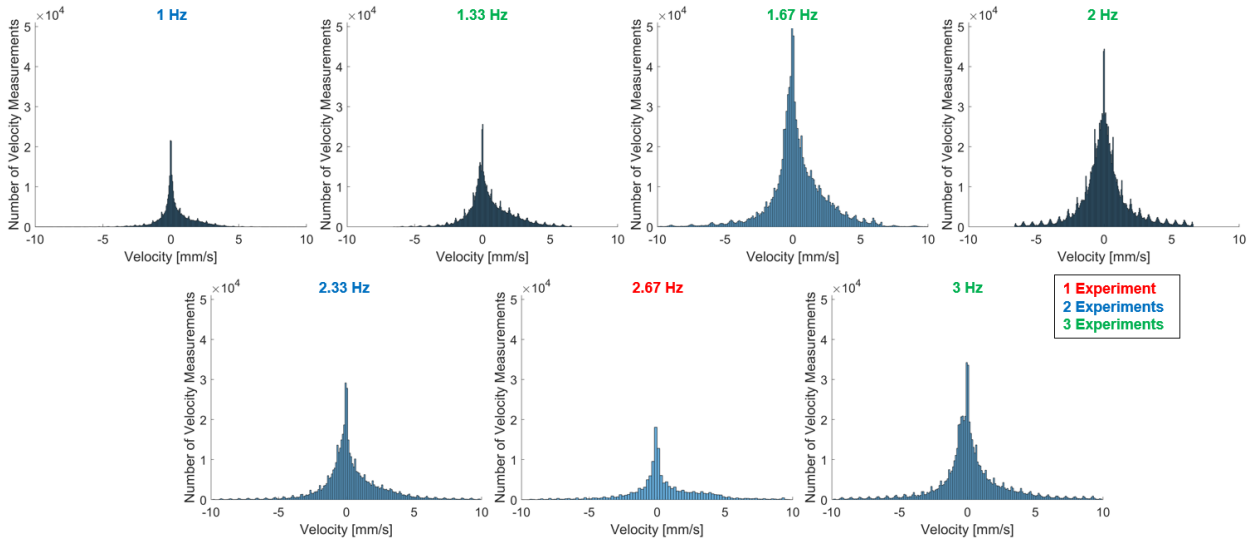

Figure 3.1: Velocity distributions at each frequency. All distributions combine three datasets (green titles), except for 1 Hz and 2.33 Hz with two datasets (blue titles), and 2.67 Hz with one dataset (red title). All axes have identical scales.

All of the distributions are highly peaked at zero. This is likely due to the oscillatory motion of flow in the microfluidic channel. It appears that the velocity measurements are between -5 mm/s and 5 mm/s for pumping frequencies 1-2 Hz and between -10 mm/s and 10 mm/s for higher pumping frequencies (Figure 3.2). The distributions appear either symmetric or slightly skewed right, which suggests that there is either no bulk flow or some forward bulk flow respectively, and that there was no backward bulk flow. The total number of measurements trends with the number of experiments combined, though the distribution for 1.33 Hz is shorter than expected. The regularly spaced, small peaks throughout the distribution are a result of a half-pixel bias in the particle tracking code.

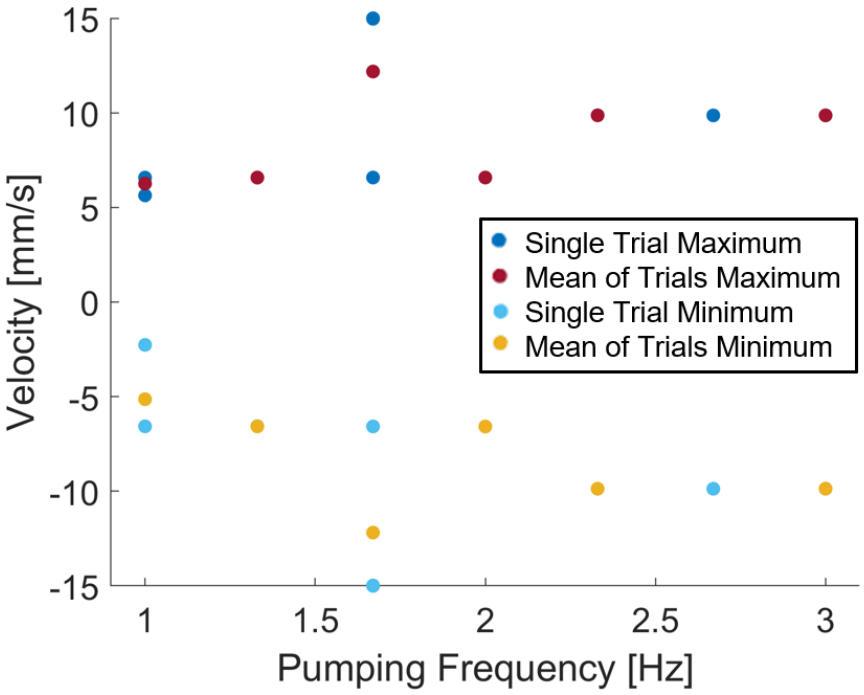

Figure 3.2: Minimum and maximum instantaneous velocity measurements along the long axis of the lower channel. Dark blue and light blue points correspond to maximum and minimum values respectively for single experiments. Red and yellow points corresponded to the average of maximum and minim values respectively for multiple trials at the same pumping frequency.

3.1.2 Moments of the Velocity Distributions

We can quantify measures of the velocity distributions using the moments of the distributions. The mean, standard deviation, skewness, and kurtosis of each velocity distribution are plotted in Figure 3.3.

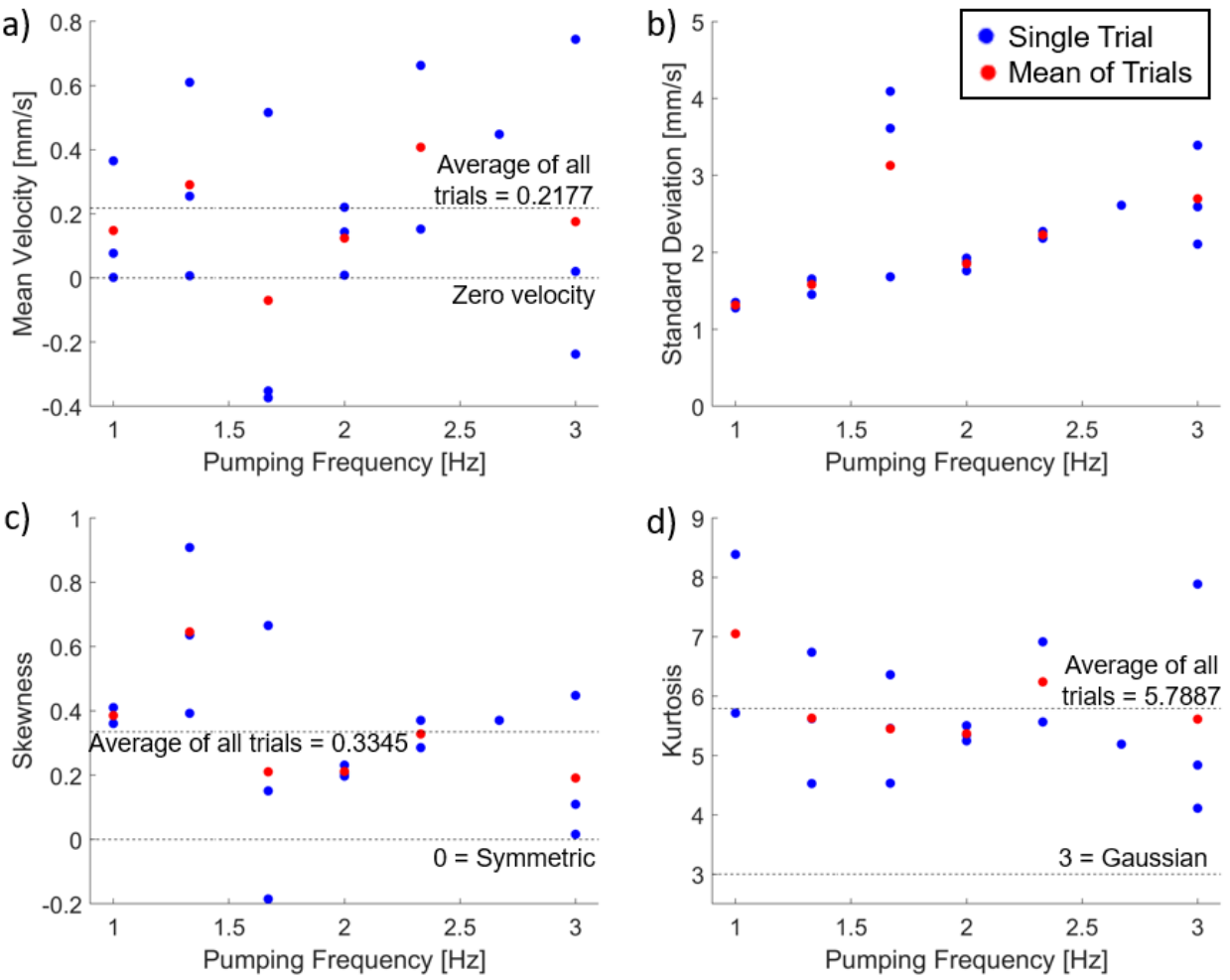

Figure 3.3: Moments of the velocity distributions at varying pumping frequencies. Blue points correspond to values from single experiments. Red points correspond to the average of multiple trials at the same pumping frequency. Labeled black dashed lines correspond to the mean over all experiments: 0.2177 mm/s for (a), 0.3345 for (b), and 5.7887 for (c). Additional black dashed lines serve as references to a mean (a) and skewness (c) of zero, and a kurtosis of three (d).

The first moment of the distributions, the mean, is shown in Figure 3.3a. The mean velocities do not appear to vary with pumping frequency. The average velocity across all

frequencies is 0.2177 mm/s, and the mean velocities measured range between -0.3735 mm/s and 0.7441 mm/s. The average velocity across all frequencies is positive, meaning the average velocity is in the forward direction.

The second moment of the distributions is the variance. The standard deviation, which is the square root of the variance, is shown in Figure 3.3b. The standard deviation σ measures the spread of a distribution and is computed as

$$\sigma = \sqrt{\frac{1}{N}\sum_{i=1}^{N}(x_i - \mu)^2} \tag{3.1}$$

where N is the number of instantaneous velocity measurements, μ is the mean of all velocity measurements, and the summation is over each individual velocity measurement x_i. For a Gaussian distribution, a low standard deviation indicates that the measurements are close to the mean while a high standard deviation indicates that the measurements are spread away from the mean. The standard deviation appears to increase linearly with pumping frequency, meaning the measurements are moving farther away from the mean as the pumping frequency increases. There are therefore more measurements at greater magnitude velocities as the pumping frequency increases.

The third moment of the distributions is the skewness, shown in Figure 3.3c. Skewness is a measure of a distribution's symmetry. The skewness s is computed as

$$s = \frac{1}{\sigma^3}\sum_{i=1}^{N}\frac{(x_i - \mu)^3}{N}. \tag{3.2}$$

The skewness of a distribution can be positive, negative, or zero with a positive value indicating that the distribution that is skewed right, a negative value indicating that the distribution is skewed left, and zero indicating the the distribution is perfectly symmetric about the mean. The velocity distributions trend slightly toward positive skewness values

with a mean skewness between all measurements of 0.3345. This means that the distributions tend to have more measurements of high magnitude forward velocities than of high magnitude backward velocities. The positive skewness could also suggest that there is a bulk forward flow.

The fourth moment of the distributions, kurtosis, is shown in Figure 3.3d. Kurtosis is a measure of how peaked a distribution is and of how much of a distribution is in the tails. The kurtosis k is computed as

$$k = \frac{1}{\sigma^4} \sum_{i=1}^{N} \frac{(x_i - \mu)^4}{N}. \tag{3.3}$$

The kurtosis of a Gaussian distribution is 3, so the excess kurtosis of a distribution is defined as the kurtosis less three. A Gaussian distribution is expected if the particle motion is purely diffusive. The kurtosis values measured are all greater than three, and thus all have a positive excess kurtosis. Distributions with a positive excess kurtosis are referred to a leptokurtic and are more peaked and have fatter tails than a Gaussian. The mean kurtosis between all measurements is 5.7887, or an excess kurtosis of 2.7887. This means that the velocity distributions are more peaked and have more measurements toward the maximum and minimum velocities than would be found for a Gaussian.

3.1.3 Comparison of Oscillations and Bulk Flow

Plotting the average position of tracer particles over time gives a picture of the fluid motion in the lower microfluidic channel. Plots of average particle position vs. time for one experiment at each pumping frequency tested are shown in Figure 3.4. Plots for all experiments in this frequency range are shown in Appendix A. Only position along the long axis of the channel is considered since flow in the microfluidic device is laminar. The initial position of the particles is set to zero for all plots. Positive position values indicate that particles are forward of the initial position, with the forward direction being the direction of the pumped flow.

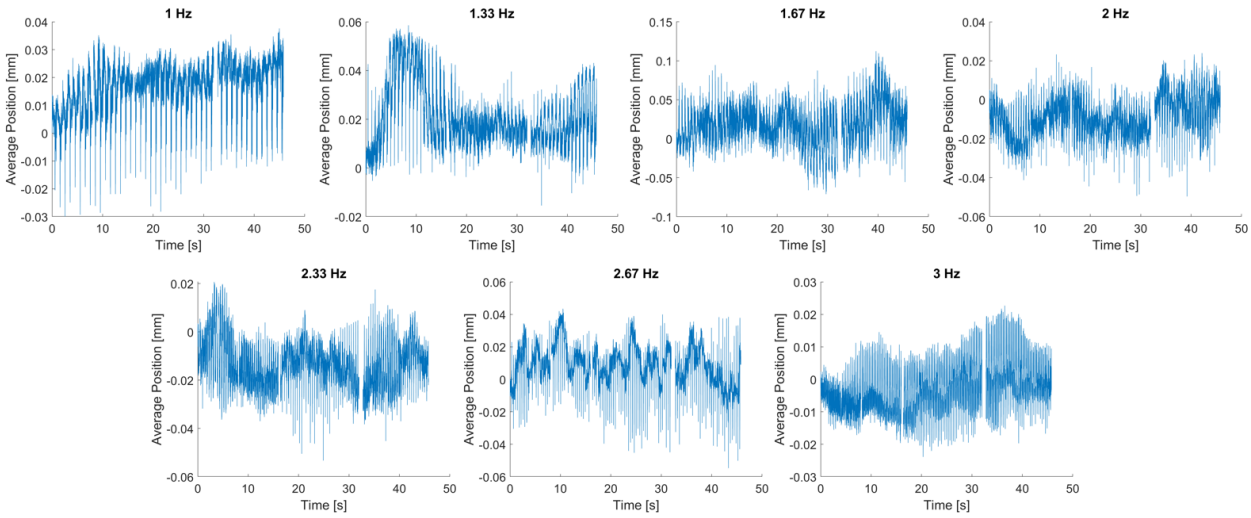

Figure 3.4: Average position of particles vs. time for each pumping frequency. Results from one experiment for each frequency are shown. Results for all experiments are shown in Appendix A.

The plots show that motion in the microfluidic channel is oscillatory on short timescales. This is expected from analytic solutions of peristaltic flow and is supported by experimental flow measurements in live mice [16]. On longer timescales, the slope of the plots gives the bulk motion. Positive slopes indicate forward bulk flow in the direction of pumping, negative slopes indicate negative bulk flow, and no slope indicates that there is no bulk flow. There does not appear to be any clear trend in the bulk flow as pumping frequency increases from these plots. While there are segments of positive slope, or forward bulk flow, in all of the plots, some plots have segments of negative slope, or backward flow, and zero slope, or no flow. By eye it appears that positive slopes, or bulk forward flow, are most prevalent.

3.2 Root-Mean-Square Speed

Computing the root-mean-square speed quantifies trends in the characteristic fluid speed over different pumping frequencies. The RMS speed is a statistical average of of the speeds of particles in a system and is often used in statistical mechanics. RMS speed is computed by squaring each instantaneous velocity measurement, finding the mean of those squared values,

and taking the square root of that mean. The RMS speed is always positive and therefore only takes into account the magnitudes of the instantaneous velocity measurements.

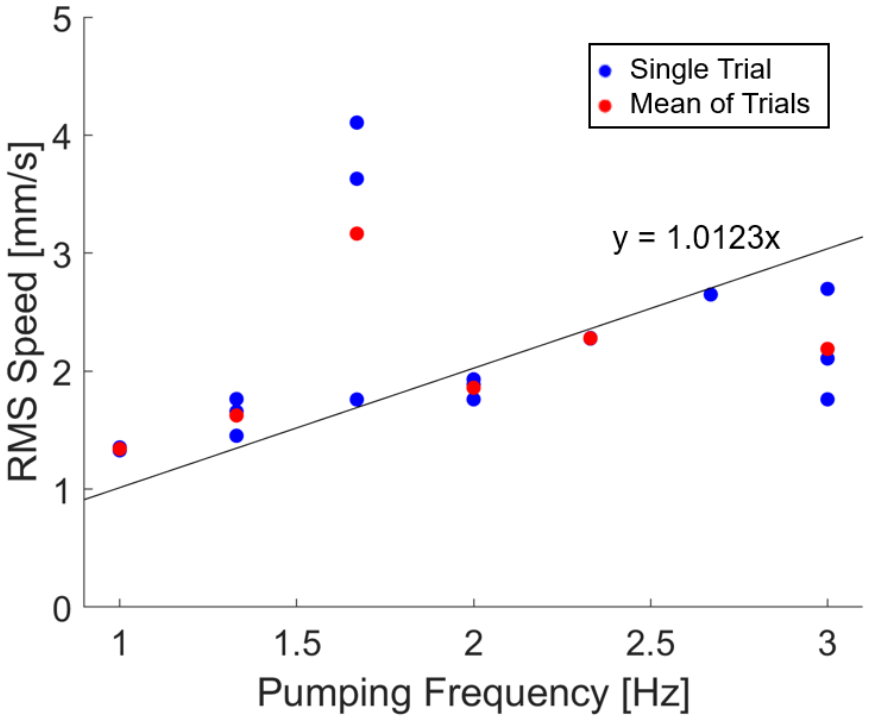

Figure 3.5: Root-mean-square speed along the long axis of the lower channel. Blue points correspond to values from single experiments. Red points correspond to the average of multiple trials at the same pumping frequency. The black line corresponds to a linear fit with the intercept fixed at zero and a slope of 1.0123 mm/s per hz.

The RMS speed of particles in the lower microfluidic channel for pumping frequencies from 1-3 Hz is shown in Figure 3.5. The RMS speed appears to increase linearly as the pumping frequency increases, meaning the typical speed in the lower channel is increasing as the pumping frequency increases. This agrees with experimental results showing that perivascular transport is greater in rats with high heart rates compared to rats with low or no heart rate [24]. A linear fit with the intercept fixed at zero has a slope of 1.0123 mm/s per hz. The RMS speed may be becoming asymptotic as the frequency approaches 2.67 and 3 Hz, though data a higher frequencies is needed to confirm this apparent trend. No information about the direction of flow can be inferred from the RMS speed alone since only the magnitudes of the velocity measurements are preserved in the calculation.

3.3 Comparison with the Membrane Motion

The average position of particles within the microfluidic channel can be compared to the membrane motion quantitatively by measuring a phase angle. Both the waves propagating through the membrane and the oscillatory motion of particles in the microfluidic channel are cyclic processes, and therefore are sinusoidal in time. The phase angle is a measure of the offset between these two sinusoidal processes in time compared to the frequency of the processes.

For two sine waves at the same frequency, the phase angle between them measures the time distance between equivalent points on the two wavelengths converted into radians, with the time for a full period being equivalent to 2π radians. The phase angle can range from zero to 2π, where the sine waves with either of these phase angles have no phase offset. In the middle of this range, sine waves with a phase angle of π are completely out of phase.

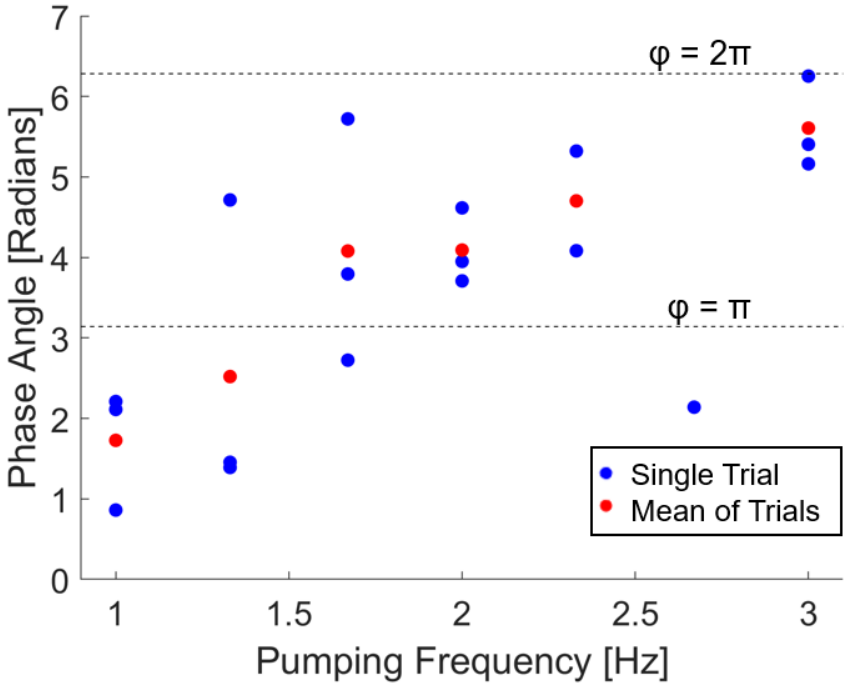

Figure 3.6: Phase angle comparisons between the approximate pumping waveform and the peak average forward position along the long axis of the lower channel. Blue points correspond to values from single experiments. Red points correspond to the average of multiple trials at the same pumping frequency. Black dashed lines correspond to angles of π and 2π.

To produce sine waves for the membrane waveform over time, we use the movement of rollers in the peristaltic pump head as a proxy (see Section 2.3.3 for rationale). The approximate membrane waveform is compared to average particle position vs. time plots (Figure 3.4). The oscillations in the average particle positions produce sinusoidal waves at approximately the same frequency of the membrane waveform. The cameras capturing these two motions are simultaneously triggered for each experiment, and therefore the times between peaks in the membrane waveform and peaks in the average forward position can be directly compared to measure the phase angle between them.

Figure 3.6 shows the results of measuring the phase angle between the membrane and particle position for each experiment. The phase angle appears to be increasing with pumping frequency toward 2π, or approximately 6.28. There is some variation of phase angles measured between each experiment, which may be from noise in the position vs. time data. Additionally, the phase angle measured for 2.67 Hz is much lower than the trend. As the pumping frequency approaches 3 Hz, the trend of the phase angles approaches 2π, or fully in phase. Measurements at higher pumping frequencies are needed to better understand the behavior of this trend. It is possible that the phase angle is asymptotic near 2π at higher frequencies, or that the phase angle follows a cyclical pattern between being in and out of phase as the pumping frequency varies. Results over broader range of frequencies are needed to further resolve this trend.

Chapter 4

Analysis of Results

4.1 Utility of 2D Particle Tracking

4.1.1 Limitations For Tracking High Particle Velocities

The 2D particle tracking code used (see Section 2.4.1) works by stringing together points from a scrambled list of coordinates and frame numbers, corresponding to all of the identified particle centroid peaks, into tracks. There are multiple parameters used to accomplish this, including the minimum length of any one track and the maximum number of frames between centroid coordinates strung together into a track. The most crucial of these parameters is the maximum displacement, which determines the maximum pixel radius within which two centroid coordinates can be connected from frame to frame. Increasing the maximum displacement increases the computation time as more centroids become candidates to join a track. When the computational time needed is deemed excessive by the code, an "excessive combinatorics" error is issued and the code stops.

The maximum displacement parameter becomes an issue when particles are moving at higher instantaneous speeds, and therefore with larger displacements between frames, than can be processed by the particle tracking code. A goal of this project was to expand the range of pumping frequencies tested. Previous experiments by Quirk [43] also used pumping frequencies from 1-3 Hz, corresponding to a range of typical human heart rates. Interest in expanding this range to higher frequencies was motivated by a desire to better understand how the measures described in the results relate to pumping frequency. The range of frequencies tested, 1-12 Hz, was motivated by typical human (1-3 Hz), rat (4-8.33 Hz), and mouse heart rates (8.33-11.67 Hz). All three species are used in studies of the

glymphatic system. Unfortunately, datasets for frequencies above 3 Hz could not be tracked with the 2D particle code due to the high maximum particle displacements between frames. Even still, particle tracking was difficult for some datasets using pumping frequencies of 2.33 Hz and 2.67 Hz.

4.1.2 Capturing Maximum Displacements

Looking at the trend of maximum and minimum instantaneous velocities vs. pumping frequencies (Figure 3.2), there is a clear shift where data from frequencies of 1-2 Hz have very similar maximum and minimum values while data from frequencies 2.33-3 Hz have very similar maximum and minimum values that are slightly greater in magnitude than the 1-2 Hz group. When particle tracking was run for these datasets, the maximum displacement parameter was set to 10 pixels for 1-2 Hz and 15 pixels for 2.33-3 Hz. This correlation incited suspicion that the maximum displacement parameter set may be limiting the maximum and minimum instantaneous velocities than can be measured.

To test this theory, we reran the 2D particle tracking using increasing maximum displacement values for a single dataset taken with a pumping frequency of 1 Hz. The tracking was run with maximum displacement values of 10 pixels, 20 pixels, 30 pixels, and 33 pixels, the maximum value that could be used without receiving an "excessive combinatorics" error. The results of these tests are summarized in Table 4.1. We found that the maximum and minimum instantaneous velocities measured are consistently very similar to the maximum and minimum possible values than can be measured from the parameter set. Therefore, the maximum and minimum velocity values measured using 2D particle tracking appear to be an artifact of the maximum displacement parameter chosen and not a result of any physical differences in the datasets.

The velocity distribution appears to be affected little by increasing the maximum displacement parameter however. The distribution of velocity measurements is largely centered around the mean, so changes in the maximum displacement parameter primarily affect the

Values	10 pixels	20 pixels	30 pixels	33 pixels
Max displacement set [mm]	0.000658	0.01316	0.01974	0.02171
Max possible speed [mm/s]	6.58	13.16	19.74	21.71
Max measured velocity [mm/s]	6.5688	13.1500	19.7360	21.6995
Min measured velocity [mm/s]	-6.5677	-13.1406	-19.7185	-21.6901
Mean [mm/s]	0.0771	0.0501	0.1427	0.1493
Standard deviation [mm/s]	1.3507	2.2848	2.9501	2.9255
Skewness	0.3605	-0.0675	0.6727	0.9425
Kurtosis	8.3840	12.5613	20.1050	23.1663
RMS speed [mm/s]	1.3529	2.2854	2.9535	2.9292

Table 4.1: Summary of results from adjusting the maximum displacement parameter for a sample at 1 Hz. The maximum and minimum instantaneous velocities measured are highly influenced by the maximum possible values set by maximum displacement parameter. However, since the parameter primarily affects the tails of the velocity distribution, the statistical measures are largely unaffected.

tails and preserve the bulk of the behavior (Figure 4.1). The velocity distribution from using a maximum displacement of 10 pixels has fewer total velocity measurements than the three higher values tested and therefore may be excluding some particle motion. The velocity distributions for the higher three maximum displacement values are nearly identical. This difference is highlighted by the slightly lower standard deviation, skewness, kurtosis, and RMS speed values measured for the 10 pixel distribution. All four distributions have roughly the same shape with the majority of behavior captured regardless of the maximum displacement parameter, and the trends of measured statistical values vs. pumping frequency observed in this project should hold regardless of the particle tracking limitations. Also, the mean, standard deviation, and RMS speed are all very similar when using a maximum displacement of 20 pixels or above.

Additionally, changing the maximum displacement parameter may alter the values of average particle position vs. time and average particle displacement vs. time peaks. Since the velocity distributions are capturing the majority of particle behavior, the parameter should not affect the times at which these peaks occur. Therefore, the trends of phase angles between pumping and position and between pumping and displacement should also be unaffected by this parameter.

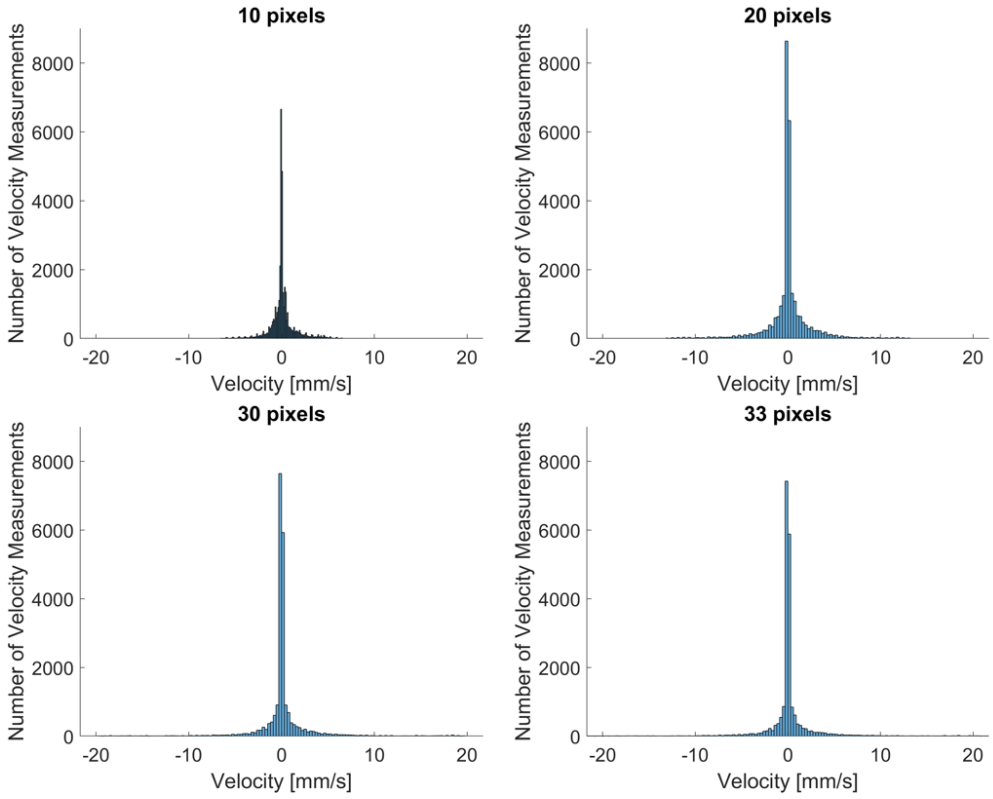

Figure 4.1: Velocity distributions for a 1 Hz dataset tracked with four different maximum displacement parameters. The maximum displacement parameter primarily affects the tails of the distribution, while most velocity measurements are centered around the mean. The velocity distribution is therefore largely unaffected by increasing the maximum displacement parameter. All axes have identical scales.

4.2 Induced Flow

Trends in the statistical moments of the velocity distributions as well as in the RMS speed provide evidence of a bulk forward motion that is increasing in speed as pumping frequency increases (Figure 3.3). For pumping frequencies from 1-3 Hz, the skewness of the velocity distribution is generally positive with a mean skewness between all distributions of 0.3345. This means that the distributions are skewed right and that there are more measurements of high magnitude forward velocities than of high magnitude backward velocities. Additionally, the standard deviation of the velocity profiles increases with pumping frequencies. This means that the velocity distributions have a greater spread toward higher magnitude velocities as the pumping frequency increases. Together, the positive skewness

and increasing standard deviation suggest a bulk forward flow that increases in magnitude as the pumping frequency increases.

The increasing magnitude of bulk flow with pumping frequency is additionally supported by the increasing RMS speed of particles as frequency increases (Figure 3.5). These results contradict previous results from Quirk [43] using a very similar microfluidic device design. They found that the RMS speed decreased exponentially over the same pumping frequency range. However, our results agree with experimental evidence showing rats with high heart rates have significantly greater periarterial transport than rats with low or no heart rate [24].

4.3 Comparison with Peristaltic Pump

The phase angle separation between the approximate membrane waveform and the peak forward particle motion increases with the pumping frequency (Figure 3.6). The phase angles measured range from 0.8612 radians for a sample at 1 Hz and 6.2530 radians for a sample at 3 Hz. The two signals are completely in phase when the phase angle is zero or 2π. For reference, 2π is equivalent to 6.2832 radians. In this range of pumping frequencies, the phase angle increases and approaches 2π. Based solely on these results, it is unclear how this trend will develop with higher pumping frequencies, whether it will saturate or vary periodically.

Experiments in live mice measure a phase angle between periarterial oscillations and arterial wall velocity of 6.1610 radians [16], which is similar to our maximum phase angle measured. This suggests that the phase angle may saturate with frequency near 2π rather than vary periodically.

Theoretical models can replicate a phase angle agreeing with experimental results by applying boundary conditions analogous to an RC circuit [54]. A simple representation of arterial pulsations is of a source, the heart, that produces a volume flow rate (Figure 4.2a). Using this simple theoretical model gives a phase angle of 4.7124, which does not agree with experimental results. This simple representation considers periarterial pumping that is uncoupled from other fluid pathways. A more realistic model considers this coupling,

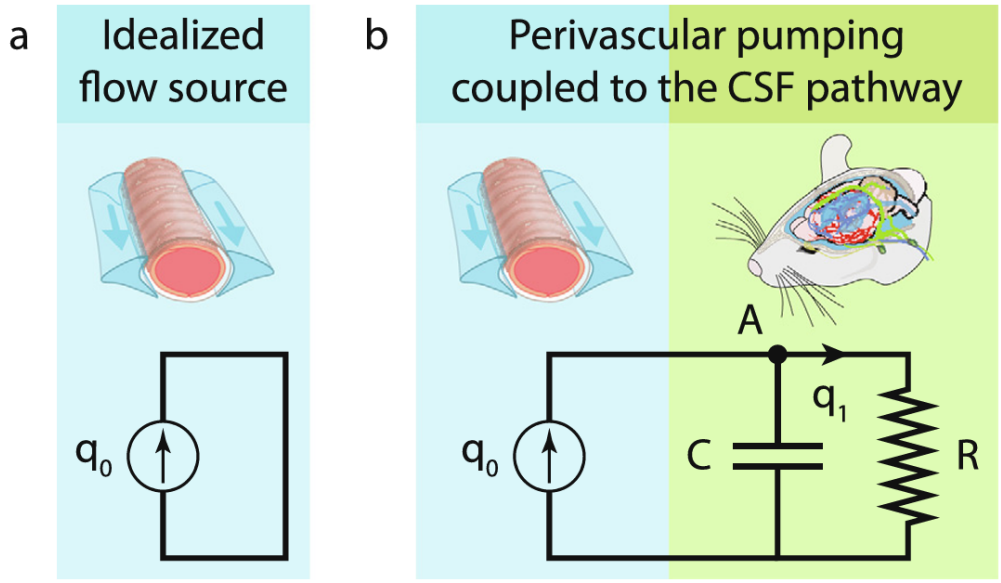

Figure 4.2: Using an RC circuit to model boundary conditions for periarterial flow driven by arterial pulsations. (a) Envisioning periarterial flow using the heart as an idealized flow source, uncoupled from other fluid pathways. (b) Including resistance and compliance components, characterizing periarterial flow that is coupled to other fluid pathways [54].

which can be done by introducing resistance and compliance parameters. The resistance of a pathway is the pressure difference over the pathway divided by the volume flow rate through it. This is analogous to electrical resistance, which is the voltage over a component divided by the current through it. The t The compliance is the flow rate through the pathway divided by the rate of change of the pressure difference across the pathway. This is similarly analogous to electrical capacitance, which is the current through the component divided by the rate of change of the voltage difference across the component.

This analogy can be extended to the flow rate for Poiseuille flow

$$q = \frac{2h^3 \Delta p}{3\eta l} \tag{4.1}$$

derived in Section 1.2.1. The flow rate q is analogous to an electrical current, the pressure drop Δp is analogous to voltage, and the remaining term $2h^3/3\eta l$ is analogous to electrical resistance. The arterial wall is analogous to an electrical capacitor.

Using this theoretical RC circuit model gives a phase angle of 6.2814 radians, which matches closely with experiments in mice [16] and the upper range of our phase angle measurements. The periarterial space can be thought of as a high-pass filter, where low frequency signals are stopped by the arterial wall and high frequency signals are allowed to travel through, or pass, the arterial wall.

Chapter 5

Discussion

5.1 Transitioning to Predictive Tracking

The issues with particle tracking encountered in this project may be resolved by using an alternative particle tracking code. Predictive tracking, developed by Ouellette [55], may be better suited to process the image data from this experiment. Predictive tracking differs from the 2D tracking in how it connects the particle centroid positions into tracks. The 2D tracking code uses combinatorics to determine the most likely match between centroids in different frames given a set maximum displacement radius to search in. Predictive tracking uses a three-frame best-estimate algorithm to produce Lagrangian particle tracks [56]. Similar to the 2D tracking, this method works on the assumption that the small particles being tracked are moving as if they are a part of the fluid. Using predictive tracking may reduce the computational effort of tracking the larger frame-to-frame displacements measured in our experiments using pumping frequencies above 3 Hz.

5.2 Comparison with Previous Microfluidic Experiments

The results of this experiment differ from those of Quirk [43], who used a similar microfluidic device design. Notably, Quirk observed a negative exponential relationship between RMS speed and pumping frequency. This contradicts the positive linear relationship measured in this project. The geometry between Quirk's devices and our devices is slightly different with Quirk using 300 μm tall channels while we used 250 μm tall channels. This difference may produce small changes in the results, though it does not account for a completely different trend. Another key difference between the experiments is the peristaltic

pump used. Quirk used a Longer Pump BQ50-1J peristaltic pump while we used a Longer Pump BT100-3J peristaltic pump fitted with a Longer Pump DG-1-B/D pump head. The peristaltic pump used by Quirk has limited functionality compared to the pump we used. The BQ50-1J pump is only capable of frequencies from 1-3 Hz, and the rotations per minute of the pump head cannot be directly set. In contrast, the pump we used is capable of frequencies up to 16.67 Hz, and the rotations per minute can be set to the nearest 0.1 rpm using a digital display. The peristaltic pump used in these experiments may therefore be more reliable than the pump used by Quirk. Additionally, the pump head used by Quirk has a smaller radius and four rollers, while the pump head we used has a larger radius and ten rollers. These differences in the pump head geometry may have an impact on the pumping motion.

5.3 Future Work

5.3.1 Expanding the Frequency Range

In this work, measurements were taken using pumping frequencies from 1-12 Hz with 0.33 Hz increments between each frequency tested. In total, three videos each were taken for frequencies 1-3 Hz and one video each was taken for 3.33-12 Hz. This is a large expansion of the 1-3 Hz range previously tested by Quirk [43] and includes frequencies corresponding to typical heart rates in humans (1-3 Hz), rats (4-8.33 Hz), and mice (8.33 - 12 Hz), all of which are used for experimental study of CSF flow. However, results are only shown for frequencies from 1-3 Hz due to the 2D particle tracking limitations previously mentioned (see Section 4.1.1). Expanding the frequency range is of interest for better understanding all of the trends with pumping frequency discussed in this project, though the trend with phase angles is of particular interest. The phase angle between pumping motion and average particle position increases toward 2π as the frequency increases from 1-3 Hz. If this trend holds, the phase angle will approach 2π at frequencies slightly above 3 Hz. Any further shift between the signals will cause the phase angle to drop down to zero as the signals become perfectly in

phase again. It will be interesting to see whether the phase angle will be asymptotic at 2π at frequencies beyond 3 Hz, or if the phase angle relationship is periodic with pumping frequency.

5.3.2 Extracting Particle Heights

Videos taken in the microfluidic channel show only a two-dimensional slice in the height of the channel. Particle motion in this two-dimensional slice provides information about fluid motion at the center height of the channel. However, the channel is a three-dimensional space, and acquiring information about the particles heights is needed if the data is used toward a computational model. One way to infer the particle heights is by using the apparent size of the particles in the image. All of the particles have the same diameter, so the apparent diameters over time could be mapped to the particle heights with some calibration efforts. The particle tracking code used measures a "radius of gyration" which could be calibrated to the particle heights.

A more obvious choice for taking three-dimensional images is confocal microscopy, though this method lacks the time resolution needed for measurements. Capturing a single confocal z-stack of the channel could take multiple seconds. Using the current bright field microscopy setup, we would have taken thousands of frames over this time.

Another microscopy technique which may help is holographic video microscopy [57]. This technique is similar to the apparent radius technique above wherein the relative appearances of the microspheres in a two-dimensional image is used to extract information about the heights. Instead of relative apparent particle sizes, holographic video microscopy uses diffraction patterns produced by the small particles to discern the height. The appearance of the diffraction patterns depends on the height of the particles, so the apparent patterns can be mapped to the particle heights.

5.3.3 Direct Membrane Tracking

The experiments discussed in this thesis used the motion of the peristaltic pump to approximate the waveform of the thin membrane between the microfluidic channels. A more exact method would be to directly image the motion of the thin membrane. Instead of having tracer particles in the lower channel, tracer particles could be embedded in the thin PDMS membrane, either by attaching them on the surface or manufacturing custom 100 μm thick PDMS with the beads mixed in. Simultaneous video of the pump and the thin membrane could be taken to confirm the accuracy of our membrane waveform approximation. Some troubleshooting would be needed to be able to analyze the up and down motion of the particles, and this would likely involve either the "radius of gyration" or holographic video microscopy techniques outlined in the previous section.

Appendices

Appendix A

Complete Set of Average Position vs. Time Plots

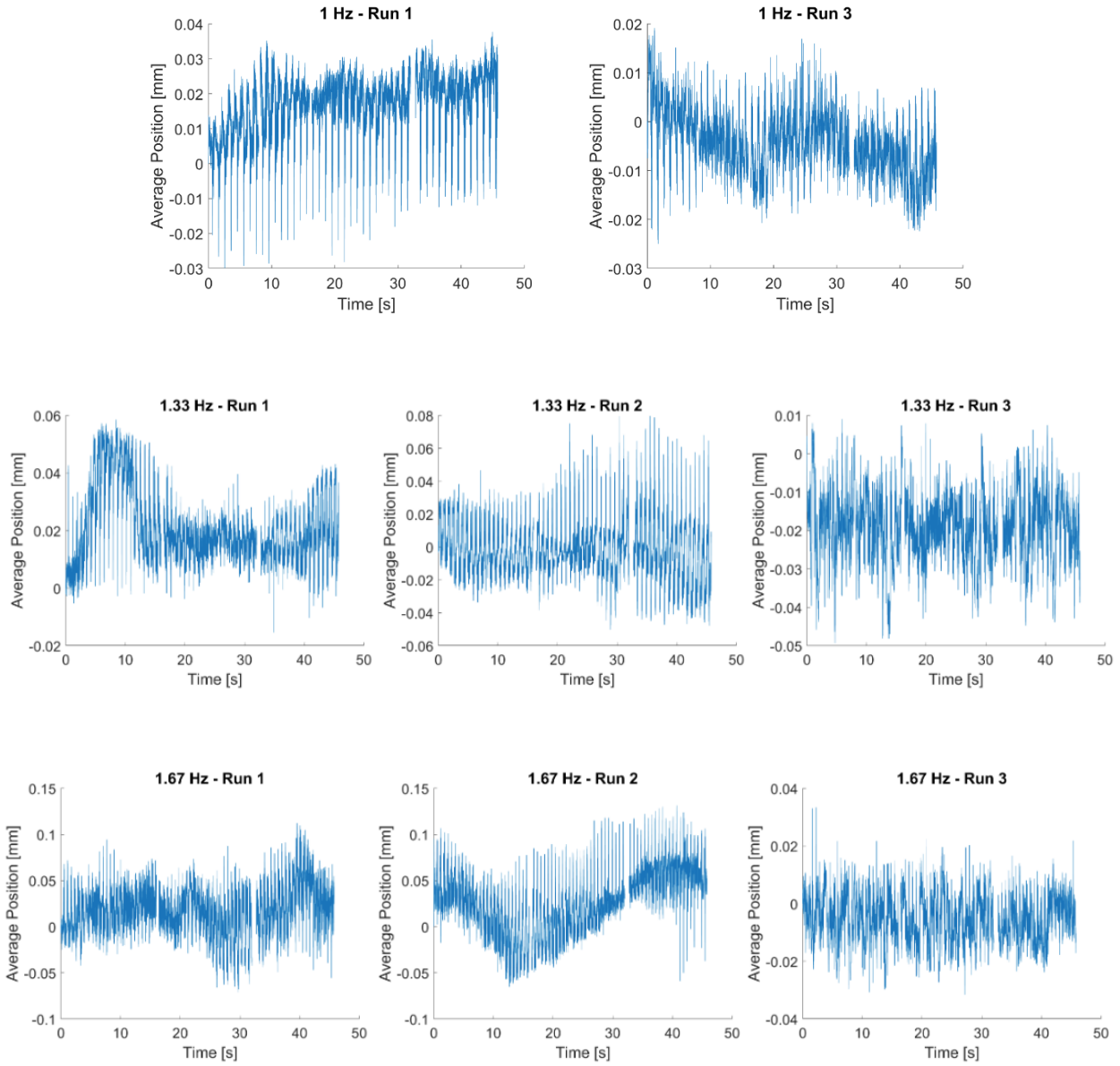

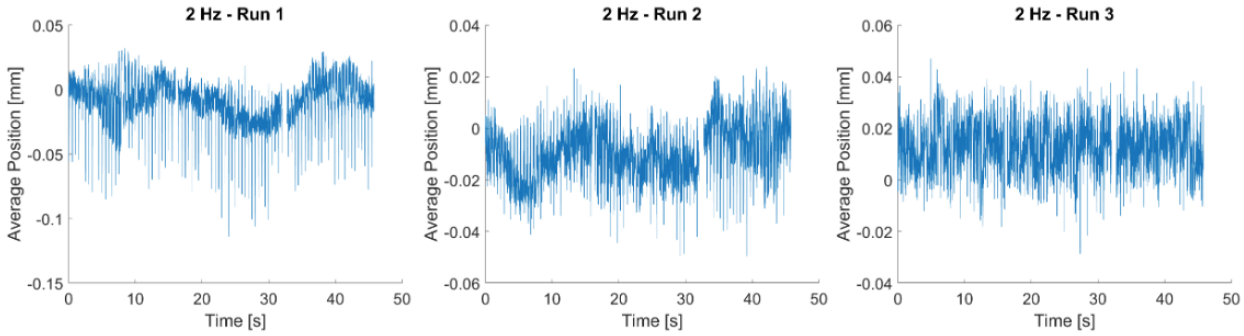
2 Hz - Run 1
Average Position [mm]
Time [s]
2 Hz - Run 2
Average Position [mm]
Time [s]
2 Hz - Run 3
Average Position [mm]
Time [s]

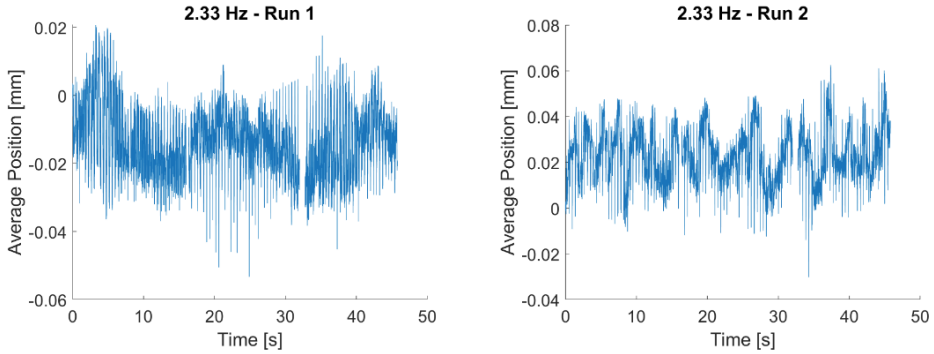
2.33 Hz - Run 1
Average Position [mm]
Time [s]
2.33 Hz - Run 2
Average Position [mm]
Time [s]

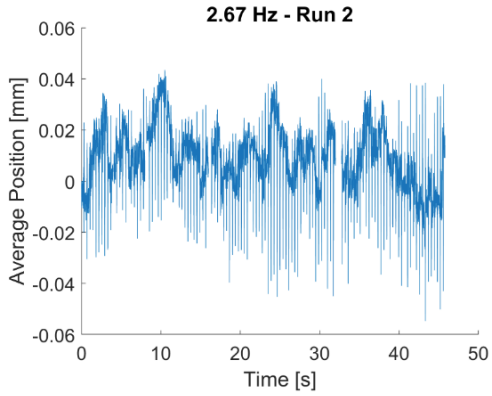
2.67 Hz - Run 2
Average Position [mm]
Time [s]

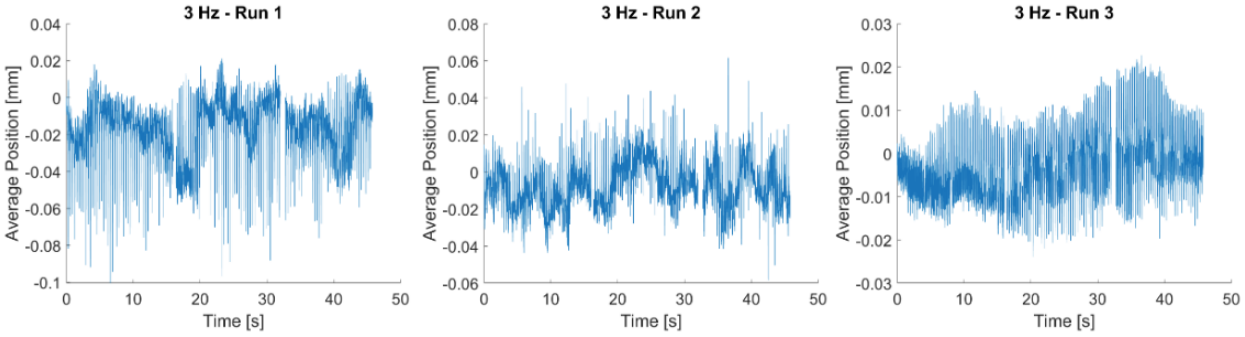
3 Hz - Run 1
Average Position [mm]
Time [s]
3 Hz - Run 2
Average Position [mm]
Time [s]
3 Hz - Run 3
Average Position [mm]
Time [s]

References

[1] D.F. Rolfe, G.C. Brown GC. "Cellular energy utilization and molecular origin of standard metabolic rate in mammals," *Physiological Reviews* **77**, 3: 735 (1997).

[2] I. Lundgaard, B. Li, L. Xie, H. Kang, S. Sanggaard, J.D.R. Haswell, W. Sun, S. Goldman, S. Blekot, M. Nielsen, T. Takano, R. Deane, M. Nedergaard. "Direct neuronal glucose uptake heralds activity-dependent increases in cerebral metabolism," *Nature Communications* **6**, 6807 (2015).

[3] L.A. Ray, J.J. Heys. "Fluid Flow and Mass Transport in Brain Tissue," *Fluids* **4**, 4: 196 (2019).

[4] J. Herz, A.J. Filiano, A.T. Wiltbank, N. Yogev, J. Kipnis. "Myeloid Cells in the Central Nervous System," *Immunity* **46**, 6: 943-956 (2017).

[5] H. Wiig, M.A. Swartz. "Interstitial Fluid and Lymph Formation and Transport: Physiological Regulation and Roles in Inflammation and Cancer," *Physiological Reviews* **92**, 3: 1005-1060 (2012).

[6] M. Loukas, S.S. Bellary, M. Kuklinski, J. Ferrauiola, A. Yadav, M.M. Shoja, K. Shaffer, R.S.Tubbs. "The lymphatic system: A historical perspective," *Clinical Anatomy* **24**, 807-816 (2011).

[7] B. Frost, M. Diamond. "Prion-like mechanisms in neurodegenerative diseases," *Nature Reviews Neuroscience* **11**, 155-159 (2010).

[8] L.C. Walker, M.I. Diamond, K.E. Duff, B.T. Hyman. "Mechanisms of Protein Seeding in Neurodegenerative Diseases," *JAMA Neurology* **70**, 3: 304-310 (2013).

[9] T.O. Wichmann, H.H. Damkier, M. Pedersen. "A Brief Overview of the Cerebrospinal Fluid System and Its Implications for Brain and Spinal Cord Diseases," *Frontiers in Human Neuroscience* **15**, 737217 (2022).

[10] M.K. Lehtinen, C.S. Bjornsson, S.M. Dymecki, R.J. Gilbertson, D.M. Holtzman, E.S. Monuki. "The choroid plexus and cerebrospinal fluid: emerging roles in development, disease, and therapy," *Journal of Neuroscience* **33**, 45: 17553-17559 (2013).

[11] S.B. Hladky, M.A. Barrand. "Mechanisms of fluid movement into, through and out of the brain: evaluation of the evidence," *Fluids and Barriers of the CNS* **11**, 26 (2014).

[12] J.J. Iliff *et al.* "A Paravascular Pathway Facilitates CSF Flow Through the Brain Parenchyma and the Clearance of Interstitial Solutes, Including Amyloid β," *Science Translational Medicine* **4**, 147 (2012).

[13] M. Nedergaard. "Garbage Truck of the Brain," *Science* **340**, 1529-1530 (2013).

[14] H. Mestre, M. Nedergaard *et al.* "Aquaporin-4-dependent glymphatic solute transport in the rodent brain," *eLife* **7**, e40070 (2018).

[15] B.A. Plog, M. Nedergaard. "The Glymphatic System in Central Nervous System Health and Disease: Past, Present, and Future," *Annual Review of Pathology: Mechanisms of Disease* **13**, 379-394 (2018).

[16] H. Mestre, J. Tithof, T. Du *et al.* "Flow of cerebrospinal fluid is driven by arterial pulsations and is reduced in hypertension," *Nature Communications* **9**, 4878 (2018).

[17] F. Troili, V. Cipollini, M. Moci, E. Morena, M. Palotai, V. Rinaldi, C. Romano, G. Ristori, F. Giubilei, M. Salvetti, F. Orzi, C.R.G. Guttmann, M. Cavallari. "Perivascular Unit: This Must Be the Place. The Anatomical Crossroad Between the Immune, Vascular and Nervous System," *Frontiers in Neuroanatomy* **14** (2020).

[18] N. Raicevic, J.M. Forer, A. Ladrón-de-Guevara, T. Du, M. Nedergaard, D.H. Kelley, K. Boster. "Sizes and shapes of perivascular spaces surrounding murine pial arteries," *Fluids and Barriers of the CNS* **20**, 56 (2023).

[19] J. Tithof, D.H. Kelley, H. Mestre, M. Nedergaard, J.H. Thomas. "Hydraulic resistance of periarterial spaces in the brain," *Fluids and Barriers of the CNS* **16**, 19 (2019).

[20] F. Min Rivas, J. Liu, B.C. Martell, T. Du, H. Mestre, M. Nedergaard, J. Tithof, J.H. Thomas, D.H. Kelley. "Surface periarterial spaces of the mouse brain are open, not porous," *Journal of the Royal Society Interface* **17**, 20200593 (2020).

[21] J.M. Wardlaw, H. Benveniste, M. Nedergaard *et al.* "Perivascular spaces in the brain: anatomy, physiology and pathology," *Nature Reviews Neurology* **16**, 137-153 (2020).

[22] A. Raghunandan, A. Ladron-de-Guevara, J. Tithof, H. Mestre, T. Du, M. Nedergaard, J.H. Thomas, D.H. Kelley. "Bulk flow of cerebrospinal fluid observed in periarterial spaces is not an artifact of injection," *eLife* **10**, e65958 (2021).

[23] B. Bedussi, M. Almasian, J. de Vos, E. VanBavel, E.N. Bakker. "Paravascular spaces at the brain surface: Low resistance pathways for cerebrospinal fluid flow," *Journal of Cerebral Blood Flow & Metabolism* **38**, 4: 719-726 (2018).

[24] P. Hadaczek, Y. Yamashita, H. Mirek, L. Tamas, M.C. Bohn, C. Noble, J.W. Park, K. Bankiewicz. "The 'Perivascular Pump' Driven by Arterial Pulsation Is a Powerful Mechanism for the Distribution of Therapeutic Molecules within the Brain," *Molecular Therapy* **14**, 1: 69-78 (2006).

[25] R.T. Kedarasetti, P.J. Drew, F. Costanzo. "Arterial pulsations drive oscillatory flow of CSF but not directional pumping," *Scientific Reports* **10**, 10102 (2020).

[26] V. Vinje, G. Ringstad, E.K. Lindstrøm, L.M. Valnes, M.E. Rognes, P.K. Eide, K.-A. Mardal. "Respiratory influence on cerebrospinal fluid flow – a computational study based on long-term intracranial pressure measurements," *Scientific Reports* **9**, 9732 (2019).

[27] L. Xie, M. Nedergaard *et al.* "Sleep Drives Metabolite Clearance from the Adult Brain," *Science* **342**, 373-377 (2013).

[28] J.-E. Kang, M.M. Lim, R.J. Bateman, J.J. Lee, L.P. Smyth, J.R. Cirrito, N. Fujiki, S. Nishino, D.M. Holtzman. "Amyloid-β Dynamics Are Regulated by Orexin and the Sleep-Wake Cycle," *Science* **326**, 3: 1005-1007 (200).

[29] P.K. Eide, V. Vinje, A.H. Pripp, K.-A. Mardal, G. Ringstad. "Sleep deprivation impairs molecular clearance from the human brain," *Brain* **144**, 3: 863-874 (2021).

[30] S. Dreha-Kulaczewski, A.A. Joseph, K.-D. Merboldt, H.-C. Ludwig, J. Gärtner, J. Frahm. "Inspiration Is the Major Regulator of Human CSF Flow," *Journal of Neuroscience* **35**, 6: 2485-2491 (2015).

[31] P.M. Gerhart, A.L. Gerhart, and J.I. Hochstein. "Munson, Young and Okiishi's Fundamentals of Fluid Mechanics," *John Wiley & Sons*, 251-259 (2016).

[32] T.E. Faber. "Fluid Dynamics for Physicists," *Cambridge University Press* 206-208 (1995).

[33] M.Y. Jaffrin, A.H. Shapiro. "Peristaltic Pumping," *Annual Review of Fluid Mechanics* **3**, 13-37 (1971).

[34] F.C.P. Yin, Y.C. Fung. "Comparison of theory and experiment in peristaltic transport," *Journal of Fluid Mechanics* **47**, 1: 93-112 (1971).

[35] S. Takabatake, K. Ayukawa. "Numerical study of two-dimensional peristaltic flows," *Journal of Fluid Mechanics* **122**, 439-465 (1982).

[36] D.H. Kelley, J.H. Thomas. "Cerebrospinal Fluid Flow," *Annual Review of Fluid Mechanics* **44**, 1: 237-264 (2023).

[37] M. Nedergaard, S.A. Goldman. "Glymphatic failure as a final common pathway to dementia," *Science* **370**, 50-56 (2020).

[38] W. Peng, T.M. Achariyar, B. Li, Y. Liao, H. Mestre, E. Hitomi, S. Regan, T. Kasper, S. Peng, F. Ding, H. Benveniste, M. Nedergaard, R. Deane. "Suppression of glymphatic fluid transport in a mouse model of Alzheimer's disease," *Neurobiology of Disease* **93**, 215-225 (2016).

[39] W. Zou, T. Pu, W. Feng, M. Lu, Y. Zheng, R. Du, M. Xiao, G. Hu. "Blocking meningeal lymphatic drainage aggravates Parkinson's disease-like pathology in mice overexpressing mutated α-synuclein," *Translational Neurodegeneration* **8**, 7 (2019).

[40] J.J. Iliff, M.J. Chen, B.A. Plog, D.M. Zeppenfeld, M. Soltero, L. Yang, It. Singh, R. Deane, M. Nedergaard. "Impairment of Glymphatic Pathway Function Promotes Tau Pathology after Traumatic Brain Injury," *Journal of Neuroscience* **34**, 29: 16180-16193 (2014).

[41] B.T. Kress, J.J. Iliff, M. Xia, M. Wang, H.S. Wei, D. Zeppenfeld, L. Xie, H. Kang, Q. Xu, J.A. Liew, B.A. Plog, F. Ding, R. Deane, M. Nedergaard. "Impairment of paravascular clearance pathways in the aging brain," *Annals of Neurology* **76**, 845-861 (2014).

[42] H. Mestre *et al.* "Cerebrospinal fluid influx drives acute ischemic tissue swelling," *Science* **367**, 6483 (2020).

[43] K. Quirk. "Microfluidic model of periarterial spaces in the glymphatic system," Bachelor's Honors Thesis, Mount Holyoke College (2020).

[44] D.J. Beebe, G.A. Mensing, G.M. Walker. "Physics and Applications of Microfluidics in Biology," *Annual Reviews* **4**, 261-286 (2002).

[45] I.G. Bloomfield, I.H. Johnston, L.E. Bilston. "Effects of Proteins, Blood Cells and Glucose on the Viscosity of Cerebrospinal Fluid," *Pediatric Neurosurgery* **28**, 5: 246–251 (1998).

[46] J.A. Schetz, A.E. Fuhs. "Fundamentals of Fluid Mechanics, 3rd ed.," *Wiley-Interscience* (1999).

[47] R.H. Perry, D.W. Green. "Perry's Chemical Engineers' Handbook, 7th ed.," *McGraw-Hill Professional*, 5-66 (1997).

[48] L.D. Landau, L.P. Pitaevskii, A.M. Kosevich, E.M. Lifshitz. "Theory of Elasticity Volume 7, 7th ed.," *Butterworth-Heinemann* 38-42 (1984).

[49] W. Megone, N. Roohpour, J.E. Gautrot. "Impact of surface adhesion and sample heterogeneity on the multiscale mechanical characterisation of soft biomaterials," *Scientific Reports* **8** (2018).

[50] N. Bouras, M.A. Madjoubi, M. Kolli, S. Benterki, M. Hamidouche. "Thermal and mechanical characterization of borosilicate glass," *Physics Procedia* **2**, 3: 1135-1140 (2009).

[51] G.B. Arfken, D.F. Griffing, D.C. Kelly, J. Priest. "International Edition University Physics," *Academic Press* 100-127 (1984).

[52] J.C. Crocker, D.G. Grier. "Methods of Digital Video Microscopy for Colloidal Studies," *Journal of Colloid and Interface Science* **179**, 298: 198 (1996).

[53] V. Genovés, L. Maini, C. Roman, C. Hierold, N. Cesarovic. "Variation in the viscoelastic properties of polydimethylsiloxane (PDMS) with the temperature at ultrasonic frequencies," *Polymer Testing* **124** (2023).

[54] A. Ladrón-de-Guevara, J.K. Shang, M. Nedergaard, D.H. Kelley. "Perivascular pumping in the mouse brain: Improved boundary conditions reconcile theory, simulation, and experiment," *Journal of Theoretical Biology* **542** (2022).

[55] N.T. Ouellette. "Particle-based measurement techniques for soft matter," in Experimental and Computational Techniques in Soft Condensed Matter Physics, *Cambridge University Press* 180-208 (2010).

[56] N.T. Ouellette, H. Xu, E. Bodenschatz. "A quantitative study of three-dimensional Lagrangian particle tracking algorithms," *Experiments in Fluids* **40**, 301–313 (2006).

[57] F.C. Cheong, B. Sun, R. Dreyfus, J. Amato-Grill, K. Xiao, L. Dixon, D.G. Grier. "Flow visualization and flow cytometry with holographic video microscopy," *Optics Express* **17**, 13071-13079 (2009).